Monitoring the incidence of *Xylella fastidiosa* in olive orchards using ground-based evaluations, airborne hyperspectral and Sentinel-2 time series imagery through 3-D radiative transfer modelling

Hornero[1*], A., Hernández-Clemente[1], R., North[1], P.R.J., Beck[2], P.S.A., Boscia[3], D., Navas-Cortes[4], J.A., Zarco-Tejada[2,4,5,6], P.J.

[1] Department of Geography, Swansea University, SA2 8PP Swansea, United Kingdom
[2] European Commission (EC), Joint Research Centre (JRC), Directorate D-Sustainable Resources, Via E. Fermi 2749 – TP 261, 26a/043, I-21027 Ispra (VA), Italy
[3] CNR, Istituto per la Protezione Sostenibile delle Piante (IPSP), via Amendola, 122/D I-70126, Bari, Italy
[4] Instituto de Agricultura Sostenible (IAS), Consejo Superior de Investigaciones Científicas (CSIC), Avenida Menéndez Pidal s/n, 14004 Córdoba, Spain
[5] School of Agriculture and Food, Faculty of Veterinary and Agricultural Sciences, University of Melbourne, Melbourne, Victoria, Australia
[6] Department of Infrastructure Engineering, Melbourne School of Engineering, University of Melbourne, Melbourne, Victoria, Australia

[*] *Corresponding author*

Submitted to Remote Sensing of Environment

Special Issue: *Integration of Space and in-Situ techniques: a new Paradigm for the Monitoring and Surveillance*

March 2019

Abstract

The outbreaks of *Xylella fastidiosa* (*Xf*) in Europe are generating considerable economic and environmental damage, and the spread of this plant pest appears to continue. Detecting and monitoring the spatio-temporal dynamics of the symptoms of diseases caused by *Xf* at large scales is key to curtailing its expansion or mitigating its impacts. This study evaluates the temporal series of airborne hyperspectral and Sentinel-2 satellite images for monitoring *Xf* infection incidence in olive orchards integrating satellite and airborne data with radiative transfer modelling and field observations. We used time-series of Sentinel-2A images collected over a two-year period to assess the temporal trends of *Xf*-infected olive orchards located in the region of Apulia, Southern Italy. First, we evaluated the sensitivity of different physiological and structural vegetation indices (VIs) to the severity and incidence of *Xf*-induced disease observed in situ. The same relationships were then evaluated using a 3D radiative transfer model to account for the temporal variations of canopy structure, understory and soil background that affect the spectral reflectance of Sentinel-2 over a grid-planted orchard. Hyperspectral images, spanning the same 2-year period as the Sentinel-2 data collected in the *Xf*-infected zone in Italy, were used for validation along with field surveys comprising more than 3000 trees across disease severity (DS) classes in 16 orchards, with varying disease-incidence (DI) levels. Among a wide range of structural and physiological vegetation indices evaluated from Sentinel-2 imagery, the temporal variation of the Atmospherically Resistant Vegetation Index (ARVI) and Optimized Soil-Adjusted Vegetation Index (OSAVI) showed superior performance for DS and DI estimation ($r^2_{ARVI}=0.74$, $p<0.001$). We estimated the difference in the spectral reflectance within each plot between 2016 and 2017 based on the VIs calculated from model simulations accounting for the temporal variations of the understory which confirm its impact, showing a Root Mean Square Error (RMSE) three times

lower than without temporal understory changes simulated. This analysis demonstrates the benefit of combining 3-D radiative transfer modelling accounting for the background variations with Sentinel-2 data to assess the spatio-temporal dynamics of *Xf* infections in olive orchards. The systematic retrieval of DI through model inversion and Sentinel-2 imagery can form the basis for operational damage monitoring worldwide. Furthermore, interpreting temporal variations of model retrievals is a critical step to detect anomalies in vegetation health.

Keywords: Sentinel-2, hyperspectral, *Xylella fastidiosa*, temporal change, radiative transfer

1. Introduction

Xylella fastidiosa (*Xf*), a plant pathogenic bacterium that can live in the xylem of more than 300 plant species is causing severe damages to multiple crops around the world (e.g. olive trees and stone fruits) (Almeida and Nunney, 2015). The first outbreak of *Xf* in Europe was detected in olive orchards in Apulia (southern Italy) in 2013 (Saponari *et al.*, 2017), and the pathogen is now officially identified in France and Spain (EFSA, 2018) and very recently (2019) in Israel. According to Saponari *et al.* (2017), olive stands can be infected for more than 5 months without noticeable symptoms. During this period, the bacterium can spread within the xylem tissue and, theoretically, cause water-related stress that may lead, among other things, to lower photosynthetic rates. The symptoms then start to become visible with a progressive increase in discolouration and defoliation of the tree crowns within a few months, and leading to their deaths within years.

Accurate detection and diagnosis of *Xf* symptoms are critical for the operational monitoring of its spread and for the reduction of losses in crop yield (Sisterson *et al.*, 2010). Recent work showed that early symptoms of *Xf* infection in olive trees are detectable through very high-resolution hyperspectral and thermal remote sensing from airborne platforms; manifested as alterations in the photoprotective mechanisms, reduction in photosynthetic activity due to pigment degradation processes, decreased chlorophyll fluorescence emission and the plant transpiration rates (Zarco-Tejada *et al.*, 2018a). Unfortunately, while airborne imaging spectroscopy permits the detection of early and even non-visible symptoms of *Xf* infection, such tree-level alterations cannot be directly detected by current satellite sensors due to their limited spectral and spatial resolution. However, we hypothesise that symptoms at intermediate and advanced stages of *Xf* diseases, visible as leaf browning, wilting, chlorosis, and desiccation of the leaves or even entire crowns, are observable in Sentinel-2 satellite data. Satellite-based monitoring of such symptoms could support the monitoring of *Xf* spread over large areas, providing the spatial distribution related to the epidemiology of *Xf* and contributing to the assesment of vegetation health by environmental managers and other end-users. Furthermore, the high revist time of up to 2-3 days at moderate latitudes of this satellite provides key temporal information about the variation in vegetation status over large areas.

Sentinel-2 images starting in 2015 are freely available and combine moderate to high spatial resolution (10 to 60 m) in 13 spectral bands, with a revisit time of five days. Given their combination of spatial, spectral, and temporal resolution, Sentinel-2 data could, in theory, be used to help monitor the spread of *Xf* over entire regions with a frequency not achievable through other means. Pre-launch studies using simulated Sentinel-2 data products demonstrated the potential of the sensor to measure several biophysical variables, such as chlorophyll content (William James

Frampton *et al.*, 2013) and leaf area index (Herrmann *et al.*, 2011). The added value of the Sentinel-2's red-edge bands has proved high accuracies when estimating chlorophyll content (Zarco-Tejada *et al.*, submitted), the fractional cover (FC) of forest canopies, the quantification of leaf area index (LAI) (Korhonen *et al.*, 2011), and for land cover-mapping (Forkuor *et al.*, 2018). Sentinel-2 data thus widen the possibility of using passive optical satellite data for vegetation monitoring, particularly in non-homogeneous and complex canopies (Lange *et al.*, 2017). The temporal resolution of Sentinel-2 offers new opportunities to understand the trends of the vegetation affected by infective agents with higher accuracy than other satellites such as Landsat (Rahimzadeh-Bajgiran *et al.*, 2018) or MODIS (Mura *et al.*, 2018). Recent studies have investigated the actual capabilities of the sensor for monitoring temporal changes in vegetation activity in different canopy types such as wetlands (Araya-López *et al.*, 2018; Whyte *et al.*, 2018), grasslands (Hill, 2013) or forests (Castillo *et al.*, 2017; Zarco-Tejada *et al.*, 2018b). To the extend of our knowledge, no studies have validated the applicability of Sentinel-2 to evaluate the spectral variations produced by the incidence of *Xf*-induced disease.

Nevertheless, the spatial resolution of Sentinel-2 causes mixed-pixel effects, which makes it challenging when attempting to separate the contribution of the different canopy scene components, such as soil, shadows, and understory, particularly in open canopies. This is relevant for the case of olive orchards, where planting densities are typically in the range of 200-2000 trees/ha, and the canopy is rarely closed (Sibbett and Ferguson, 2005). The mixture of canopy scene components hamper the scaling up of plant functional traits from pure tree crown to broader spatial extents. Furthermore, the understory and soil in these landscapes may vary considerably spatially and through time, as a result of vegetation phenology, agricultural practices, or soil dynamics impacting the multi-temporal spectral datasets.

Common approaches to assess vegetation traits from passive optical satellite observations include the use of vegetation indices and radiative transfer models (RTM). The normalised difference vegetation index (NDVI) has been widely applied for vegetation trend analysis (Beck *et al.*, 2011; Fang *et al.*, 2018; Gillespie *et al.*, 2018), and to monitor vegetation productivity in olive groves (Brilli *et al.*, 2013; Noori and Panda, 2016). Besides its strengths, the limitations of NDVI for vegetation monitoring have received much attention in the literature (Montandon, 2009; Myneni *et al.*, 1991). These limitations stem from the index's sensitivity to soil and atmospheric features, and its tendency to saturate in high-biomass environments. As a result, alternatives such as the soil-adjusted vegetation index (SAVI) (Huete, 1988), adjusted transformed soil-adjusted vegetation index (ATSAVI) (Baret and Guyot, 1991a), atmospherically resistant vegetation index (ARVI) (Huete *et al.*, 1994) or the global environment monitoring index (GEMI) (Pinty and Verstraete, 1992) have been proposed. For instance, ARVI has a similar dynamic range to NDVI, but on average is four times less sensitive to atmospheric effects than NDVI (Kaufman and Tanre, 1992a). However, the spectral mixture produced using medium resolution satellite observations inherently limits the extent to which vegetation indices can upscale field observations of plant functional traits to entire landscapes (Atzberger and Richter, 2012; Zurita-Milla *et al.*, 2015). In addition, the large effects in the spectral reflectance of the canopy produced by the variation in the understory may have important implications in the aplicability of this VI in temporal change analysis. The literature lacks studies focused on the sensitivity of VI to variations in both vegetation health and temporal change, including the contribution of changes in the understory that affect the reflectance information of Sentinel images.

RTM can overcome some of these typical limitations of purely empirical approaches, minimising the dependence of field measurements and modelling the reflectance mixture produced by the contribution of different components at medium resolutions. These two factors are essential to improve the retrieval of biophysical vegetation parameters over time. For uniform canopies, the use of 1-D RTM such as SAIL (Verhoef, 1984) has been successfully used to monitor grass and crop stress (Bayat *et al.*, 2016; Martín *et al.*, 2007). However, modelling heterogeneous and discontinuous vegetation canopies require the use of complex 3-D RTM models accounting for tree canopy structure and background effects. Previous studies have used FLIGHT to provide a 3-D representation of tree canopies to perform the spatial and spectral scaling of different biophysical variables (Bye *et al.*, 2017; Hernández-Clemente *et al.*, 2017). Still, none of these models includes the effect produced by the understory on the spectral reflectance of the canopy. The variations in understory is especially important in natural environments with high-impact in time-series data analysis over heterogeneous or sparse canopies (Assal *et al.*, 2016; Yang *et al.*, 2014). Some other RTM such as DART (Gastellu-Etchegorry *et al.*, 1996) have overcome these limitation and could particularly benefit the simulation of the canopy. On the contrary, the large number of parameters needed in this case can limit the inversion procedures (Hernández-Clemente *et al.*, 2014; Yáñez-Rausell *et al.*, 2015).

Here, we investigate the use of Sentinel-2 images for monitoring disease symptoms in *Xf*-affected olive orchards. Using field observations and multi-temporal remote sensing data we assessed i) the capability of physiological and structural vegetation indices calculated from Sentinel-2 imagery to evaluate DI and DS in *Xf*-affected olive orchards in the southern Italy infected zone, and ii) whether the application of a 3-D radiative transfer model to account for temporal changes in the soil and understory improved the prediction of *Xf* incidence based on Sentinel-2 datasets.

2. Material and methods

2.1. Study site and field data collection

The study was conducted in olive orchards (*Olea europaea* L.) located in Apulia (southern Italy, 40°30'50"N 18°01'50"E), an area where *Xf* was officially detected for the first time in October 2013 (Fig. 1). Despite phytosanitary measures, they have been unsuccessful so far in preventing the spread of *Xf* through southern Apulia, which has a temperate climate with mild winters, and a landscape dominated by olive orchards, that favour the natural spread of *Xf* (Saponari *et al.*, 2017; Strona *et al.*, 2017). By 2015, the pathogen had spread throughout a ca. 275,000 ha area in the region, and currently, it affects an area greater than 600,000 ha labelled as 'Infected zone' in Fig. 1.

Figure 1. Southern Italy with a Sentinel-2 footprint overlaid (green box, *B*), and a corresponding Sentinel 2A scene (large inset, *A*), on which airborne hyperspectral mosaics are overlaid. The three hyperspectral images were acquired from aircraft on 28 June 2016 with a micro-hyperspectral imager yielding 40 cm spatial resolution. The infected zone highlighted (red box, *C*) in the main map outlines the area where *Xylella fastidiosa* has been found as of March 2018 (*Commission Implementing Decision (EU) 2018/927*, 2018)

We carried out field surveys in 16 olive orchards located in the *Xf*-infected zone where qPCR analysis had confirmed the presence of *Xf* (Zarco-Tejada *et al.*, 2018a), making it the most likely causal agent of the symptoms. During the surveys, disease severity (DS) and incidence (DI) was assessed for 3300 olive trees. Seem (1984) defines DS as the quantity of disease which is affecting entities within a sampling unit; DI is a quantal measure, defined as the proportion or percentage of diseased entities within a sampling unit. DS thus accounts for disease severity, while incidence only considers whether a tree is affected or not. Incidence is, therefore, quicker and easier to measure, and generally more accurate and reproducible than other quantitative measures, making it usually the preferred measurement method for the detection and enumeration of disease propagation patterns (Horsfall and Cowling, 1978). Based on visual inspection, we assigned individual trees to one of five DS categories (Fig. 2) depending on the proportion of their crown affected by typical *Xf* symptoms including desiccation and discolouration of leaves and branches. DS ranged from 0, indicating the absence of symptoms, to 4 when most of the branches were dead in the crown (Table 1). DI was either 0 or 1, indicating non-symptomatic trees and symptomatic trees respectively, where non-symptomatic trees corresponded to a severity of 0 and symptomatic trees to any other severity DS>0 (Fig. 3). From these records per tree, we calculate the average of DS and DI of all trees for each orchard (DSo and DIo, respectively).

Level	Severity	Description	Desiccation	Incidence
0	Healthy	Symptomless	0%	No incidence
1	Initial severity	Few desiccated branches affecting a limited part of the canopy	> 0 ≤ 25%	Incidence
2	Medium severity	Desiccation affecting a large part of the canopy	> 25 ≤ 50%	Incidence
3	High severity	Canopy with desiccated branches uniformly distributed	> 50 ≤ 75%	Incidence
4	Very high severity	Severe tree decline	> 75%	Incidence

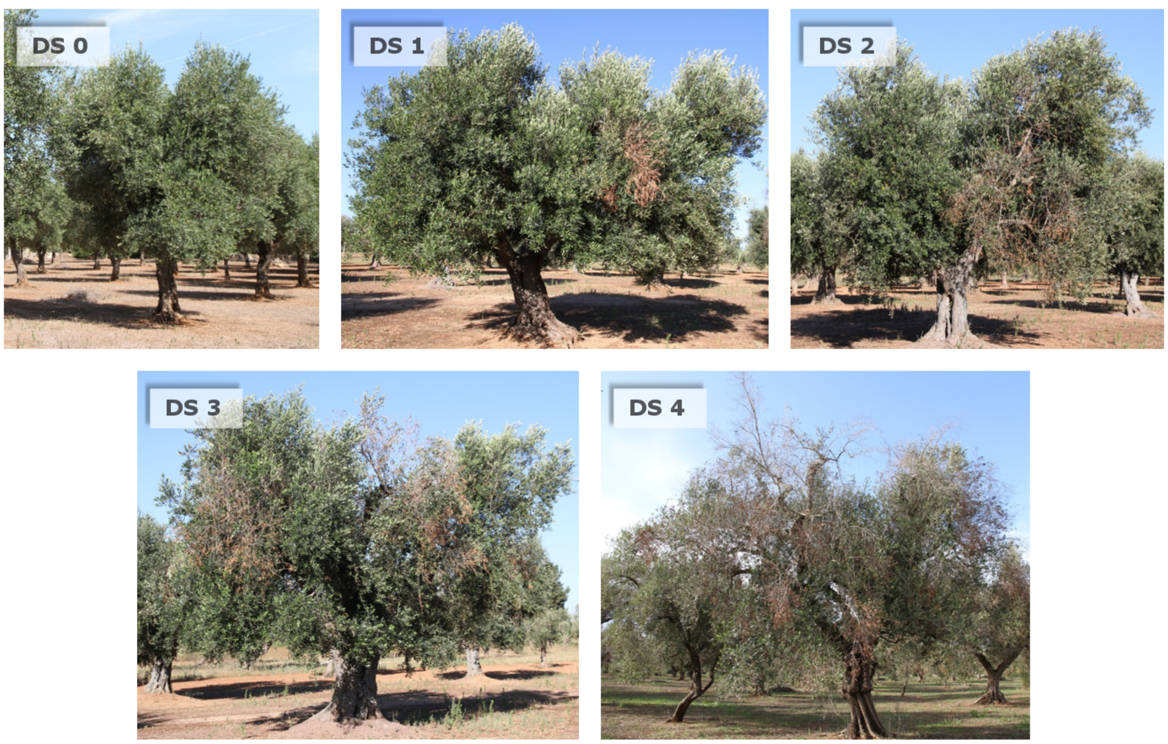

Figure 2. Examples of the five disease severity (DS) classes that olive trees (n=3300) were assigned to during a field survey in 2016 that was repeated in 2017. The classes related to the extent of severity of typical visual symptoms of *Xylella fastidiosa* ranging from apparently healthy trees (DS=0) to trees showing canopies with a prevalence of dead branches (DS = 4).

Table 1. *Xylella fastidiosa* evaluation criteria: severity and incidence crown level assignment.

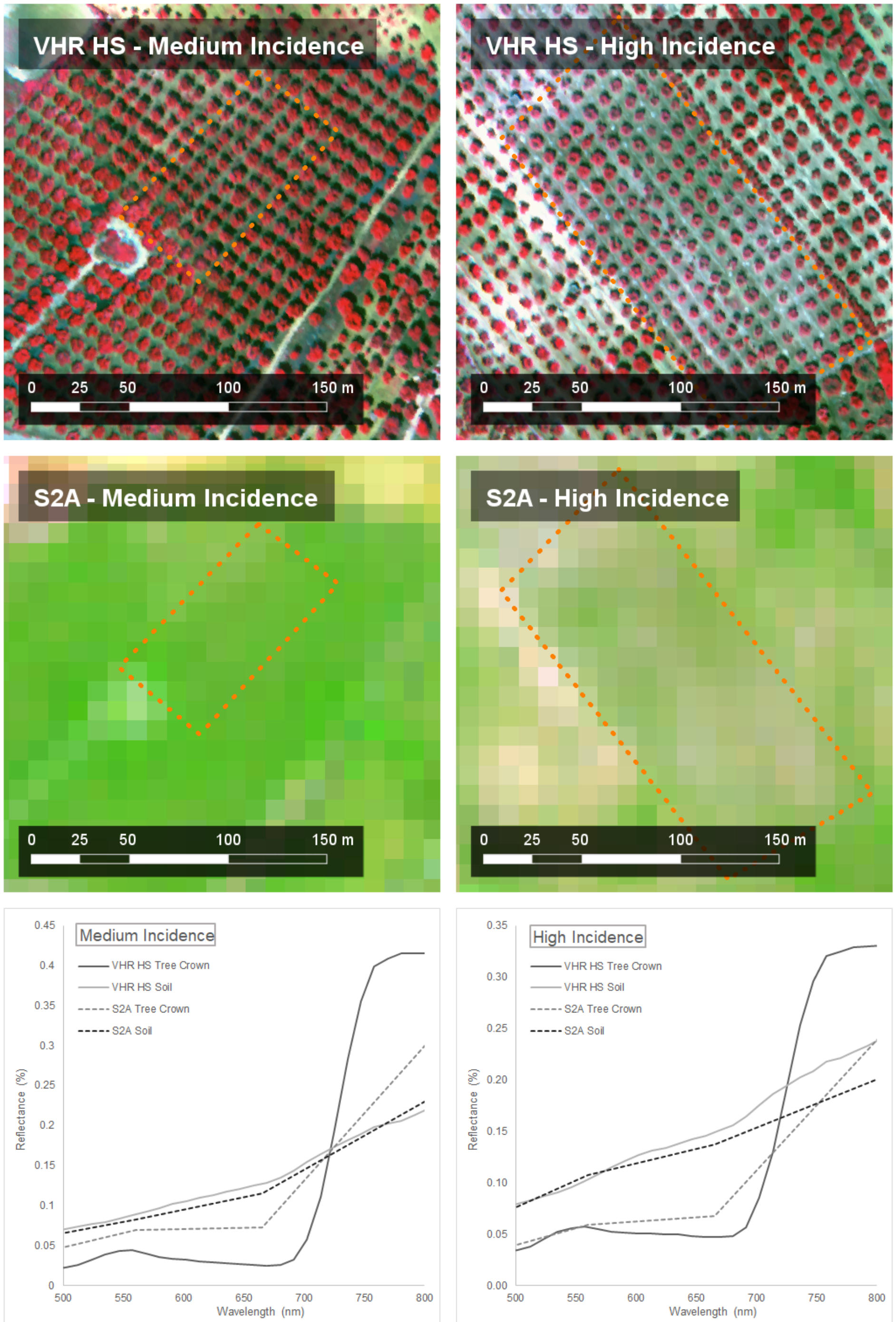

Figure 3. Example of olive orchards with medium (left panel) and high (right panel) incidence of *Xf*-related disease, viewed by an airborne high-resolution narrow-band hyperspectral camera (VHR HS, top), Sentinel-2A (S2A, middle, RGB-composite of bands B3, B2 and B4) and through their spectral signature captured by the VHR HS and Sentinel-2A (bottom).

The first field survey was conducted in June 2016, and found 48.5% of the trees to be asymptomatic; when it was repeated in July 2017, this was 15.2%. Symptomatic trees were found in all the sampled orchards in both years, with a minimum DIo of 25.0 % and 63.9 % in 2016 and 2017, respectively. This reflects the fact that all olive orchards across a very large region, that extends more than 50 km from our study sites, are infected to some degree (Fig. 1). Given the ubiquity of *Xf* there and the challenge of determining an area is *Xf*-free, a direct comparison between *Xf*-infected and *Xf*-free orchards experiencing otherwise similar environmental conditions is not possible. The relative increase of *Xf* infection in surveyed orchards, expressed as ΔDS and ΔDI, was measured based on the DSo and DIo observed between the 2016 and 2017 field surveys as:

$$\Delta DS = (DSo_{year\ n+1} - DSo_{year\ n}) / DSo_{year\ n} \qquad (1)$$

$$\Delta DI = (DIo_{year\ n+1} - DIo_{year\ n}) / DIo_{year\ n} \qquad (2)$$

where values above zero of ΔDS and ΔDI imply an aggravation of the symptoms; zero values correspond to orchards with no significant changes; and values below zero refer to a lessening of visual symptoms in an orchard.

2.2. Sentinel-2A imagery

A temporal dataset of Sentinel-2 images was used to analyse the feasibility of detecting the ΔDS and ΔDI of *Xf* infection using VI trends. The Multispectral Instrument (MSI), on board Sentinel-2A, acquires imagery at a ten-day interval under constant viewing conditions which results in 4-6 day revisit times at mid-latitudes due to the swath overlap between neighbouring orbits. The MSI measures reflected radiance in 13 spectral bands from visible and near-infrared

(VNIR) to short-wave infrared (SWIR), with images at 12-bit per channel and with a spatial resolution of 10 m (Central Wavelength (CWL) at 496.6, 560.0, 664.5 and 835.1 nm with a bandwidth of 98, 45, 38 and 145 nm, respectively), 20 m (CWL at 703.9, 740.2, 782.5, 864.8, 1613.7 and 2202.4 nm with a bandwidth of 19, 18, 28, 33, 143 and 242 nm, respectively) and 60 m (CWL at 443.9, 945.0 and 1373.5 nm with a bandwidth of 27, 26 and 75 nm, respectively).

In this study, we used the multi-temporal Sentinel-2A data available for the first two complete years after its launch in 2015. We built a multi-temporal spectral dataset from the 86 cloud-free Sentinel-2A images (Level-1C, ortho-rectified imagery expressed in top-of-atmosphere reflectance) (Richter *et al.*, 2011) available from July 2015 to August 2017. From Level-1C, the images were atmospherically corrected to generate Level-2A (bottom-of-atmosphere - surface reflectance - provided with a pixel classification mask) with Sen2Cor (version 2.3.1). Using the scene classification from Level-2A, we then filtered the data that were affected by clouds or cirrus before calculating a suite of vegetation indices.

We selected spectral VIs that are primarily sensitive to canopy structure or pigment concentration and compatible with the spectral bandset of Sentinel-2. The equations and references for each VI are shown in Table 2. More precisely, we calculated i) conventional and corrected ratio and normalised indices derived from the near-infrared and red bands such as Normalized Difference Vegetation Index (NDVI), Modified Simple Ratio (MSR), Green Normalized Difference Vegetation Index (GNDVI) and Renormalized Difference Vegetation Index (RDVI); ii) conventional soil-adjusted indices such as Adjusted Transformed Soil-Adjusted VI (ATSAVI), Optimised Soil Adjusted Vegetation Index (OSAVI) and Modified Soil-Adjusted Vegetation Index (MSAVI) and corrected versions using SWIR bands such as $OSAVI_{1510}$; iii) conventional and corrected chlorophyll vegetation indices such as Chlorophyll Index (CI), Normalized

Difference Index (NDI), Medium Resolution Imaging Spectrometer (MERRIS) Terrestrial Chlorophyll Index (MTCI), Pigment Specific Simple Ratio A (PSSRa), Sentinel-2 Red-Edge Position (S2REP), Inverted Red-Edge Chlorophyll Index (IRECI); and iv) chlorophyll indices formulated to minimise their sensitivity to structural effects based on the Chlorophyll Absorption in Reflectance Index (CARI) and its transformations into Transformed Chlorophyll Absorption Ratio Index (TCARI) & Modified Chlorophyll Absorption Ratio Index (MCARI) normalised by OSAVI in the form $^{TCARI}/_{OSAVI}$ and $MCARI_{1510}$ using SWIR bands, as formulated in Table 2. Finally, a smoothing algorithm based on Local Polynomial Regression Fitting (Cleveland *et al.*, 1992) reduced atmospheric variability and filled gaps to produce daily time-series of the indices.

Table 2. Vegetation indices derived from Sentinel-2 data included in this study and their formulations.

Vegetation index	**Equation**	**Reference**
Normalized Difference Vegetation Index	$NDVI = (R_{800} - R_{670})/(R_{800} + R_{670})$	(Rouse *et al.*, 1974)
Chlorophyll Index	$CI = \frac{R_{710}}{R_{710}}$	(Zarco-Tejada *et al.*, 2001)
Normalized Difference Index	$NDI = (R_{706} - R_{664})/(R_{704} + R_{664})$	(Delegido *et al.*, 2011)
MERIS Terrestrial Chlorophyll Index	$MTCI = (R_{754} - R_{709})/(R_{709} - R_{681})$	(Dash and Curran, 2007)
Modified Chlorophyll Absorption Ratio Index	$MCARI = ((R_{700} - R_{670}) -0.2(R_{700} - R_{550}))\left(\frac{R_{700}}{R_{670}}\right)$	(Haboudane *et al.*, 2004)
Green Normalized Difference Vegetation Index	$GNDVI = (R_{800} - R_{550})/(R_{800} + R_{550})$	(Gitelson *et al.*, 1996)
Pigment Specific Simple Ratio A	$PSSRa = \frac{R_{800}}{R_{680}}$	(Blackburn, 1998)
Sentinel-2 Red-Edge Position	$S2REP = 705 + 35\frac{\frac{R_{783} + R_{665}}{2} - R_{705}}{R_{740} - R_{705}}$	(W. J. Frampton *et al.*, 2013)
Inverted Red-Edge Chlorophyll Index	$IRECI = (R_{783} - R_{665})/(R_{705} + R_{740})$	(W. J. Frampton *et al.*, 2013)
Renormalized Difference Vegetation Index	$RDVI = (R_{800} - R_{670})/\sqrt{(R_{800} + R_{670})}$	(Roujean and Breon, 1995)
Modified Simple Ratio	$MSR = \frac{R_{800}/R_{670} - 1}{(R_{800}/R_{670})^{0.5} + 1}$	(Chen, 1996)
Transformed Chlorophyll Absorption Ratio	$TCARI = 3\left(\begin{matrix}(R_{700} - R_{670}) \\ -0.2\,(R_{700} - R_{550})\frac{R_{700}}{R_{670}}\end{matrix}\right)$	(Haboudane *et al.*, 2002)
Optimized Soil-Adjusted Vegetation Index	$OSAVI = (1 + 0.16)\ \frac{R_{800} - R_{670}}{R_{800} + R_{670} + 0.16}$	(Rondeaux *et al.*, 1996)
TCARI/OSAVI	$TCARI/OSAVI\ = \frac{\mathrm{TCARI}}{\mathrm{OSAVI}}$	(Haboudane *et al.*, 2002)
Modified Chlorophyll Absorption Ratio Index 1510	$MCARI1510 = ((R_{700} - R_{1510}) -0.2(R_{700} - R_{550}))\left(\frac{R_{700}}{R_{1510}}\right)$	(Herrmann *et al.*, 2010)

Transformed Chlorophyll Absorption Ratio 1510	$TCARI1510 = 3\left((R_{700} - R_{1510}) - 0.2\,(R_{700} - R_{550})\frac{R_{700}}{R_{1510}}\right)$	(Herrmann *et al.*, 2010)
Optimized Soil-Adjusted Vegetation Index 1510	$OSAVI1510 = (1 + 0.16)\,\frac{R_{800} - R_{1510}}{R_{800} + R_{1510} + 0.16}$	(Herrmann *et al.*, 2010)
Red Green Ratio Index	$IRG = R_{670} - R_{550}$	(Gamon and Surfus, 1999)
Perpendicular Vegetation Index	$PVI = \frac{R_{800} - a \cdot R_{670} - b}{\sqrt{a^2 + 1}}$	(Richardson and Wiegand, 1977)
Ratio Vegetation Index - Simple Ratio 800/670	$RVI = \frac{R_{800}}{R_{670}}$	(Pearson and Miller, 1972)
Adjusted Transformed Soil-Adjusted VI	$ATSAVI = a \cdot \frac{R_{800} - a \cdot R_{670} - b}{a \cdot R_{800} + R_{670} - ab + x(1 + a^2)}$	(Baret and Guyot, 1991b)
Atmospherically Resistant Vegetation Index	$ARVI = \frac{R_{800} - R_{670} - y(R_{670} - R_{450})}{R_{800} + R_{670} - y(R_{670} - R_{450})}$	(Bannari *et al.*, 1995)
Global Environment Monitoring Index	$GEMI = n(1 - 0.25n)\frac{R_{670} - 0.125}{1 - R_{670}}$ $n = \frac{2\left({R_{800}}^2 - {R_{670}}^2\right) + 1.5 \cdot R_{800} + 0.5 \cdot R_{670}}{R_{800} + R_{670} + 0.5}$	(Pinty and Verstraete, 1992)
Difference Vegetation Index	$DVI = g \cdot R_{800} - R_{670}$	(Richardson and Wiegand, 1977)
Aerosol Free Vegetation Index 1600	$AFRI1510 = R_{800} - 0.66\frac{R_{1600}}{R_{800} + 0.66 \cdot R_{1600}}$	(Karnieli *et al.*, 2001)
Aerosol Free Vegetation Index 2100	$AFRI2100 = R_{800} - 0.5\frac{R_{2100}}{R_{800} + 0.56 \cdot R_{2100}}$	(Karnieli *et al.*, 2001)

For each of the 16 orchards, we used the daily dataset of VIs to calculate the values for June 2016 and July 2017 taking the means over 2-week intervals centred on the dates of the ground measurement collection to reduce random fluctuations in time series data. We additionally calculated the temporal rate of change for each VI in the form $VI_{year=n+1}$ / $VI_{year=n}$ in order to understand the temporal trajectory of VIs as a function of the *Xf* infections. Finally, Pearson correlation analysis and *p-values,* adjusted with a Bonferroni correction to control false positives (Haynes, 2013), were used to determine the strength and statistical significance of the relationship between the in-situ measurements of *Xf* impact, i.e. ΔDI and ΔDS, and the rate of change of VIs derived from Sentinel-2 data.

2.3. Airborne hyperspectral images

For validation purposes, we collected very high-resolution images (Fig. 3) on 28th June 2016, and 3rd July 2017, using a micro hyperspectral imager – Micro-Hyperspec VNIR model (Headwall Photonics Inc., Fitchburg, MA, USA) – on board a Cessna aircraft. Visible and near-infrared spectral regions (400-885 nm) were covered by operating the sensor with 260 bands and a radiometric resolution of 12 bits at 1.865 nm CWL interval, yielding 6.4 nm full-width at half-maximum (FWHM) spectral resolution with a 25-µm slit. The acquisition frame-rate on board the aircraft was 50 frames per second with an integration time of 18 ms; with a focal length of 8 mm, an angular field of view (FOV) of 49.82° was produced (instantaneous (IFOV) of 0.93 mrad). More platform details and sensor configuration can be found in Zarco-Tejada *et al.* (2013). The hyperspectral sensor was radiometrically calibrated in the laboratory with an Ulbricht sphere (CSTM-USS-2000C Uniform Source System from LabSphere, North Sutton, NH, USA) by calculating coefficients derived from the calibrated light source in four illumination levels. The atmospheric correction was carried out using the total incoming irradiance simulated with the SMARTS model (Gueymard, 1995, 2001), which allowed the conversion of radiance values to reflectance. The model was fed with data from a weather station (WX510 from Vaisala, Vantaa, Finland) and a MICROTOPS II solar photometer (Solar LIGHT Co., Philadelphia, PA, USA). Hyperspectral imagery was ortho-rectified with PARGE (ReSe Applications Schläpfer , Wil, Switzerland) using inputs from an inertial measurement unit (MTiG from Xsens, Enschede, Netherlands) installed on board and synchronized with the imager; image correction and data pre-processing are described in detail in Hernández-Clemente *et al.* (2012) and Zarco-Tejada *et al.* (2016).

The hyperspectral images had a ground resolution of 40 cm, allowing us to distinguish individual olive tree crowns from the background made up of soil and understory vegetation. We used the hyperspectral images to evaluate the contribution of the background in the relationship between ΔDI and the rate of change of VIs derived from Sentinel-2 data. To do this, we calculated for each orchard the hyperspectral vegetation indices separately for the background areas surrounding the trees – with a five metres radius from its centroid and masking the crown by segmentation – and for the tree crowns only.

We also used the very high-resolution images as ground-truth for model parametrisation, detailed in the next section, following the methodology proposed by (Zarco-Tejada *et al.*, 2019) using scene components extracted from airborne hyperspectral images. Fig. 4 shows a strong correlation between VIs derived from Sentinel-2 and hyperspectral images over the 16 olive orchards in both 2016 (r^2=0.86, $p<0.001$ for NDVI and r^2=0.78, $p<0.001$ for OSAVI) and 2017 (r^2=0.68, $p<0.001$ for NDVI and r^2=0.65, $p<0.001$). Hence, the consistency between the two datasets enables the use of the high-resolution imagery as ground-truth for model parametrisation (Fig. 4).

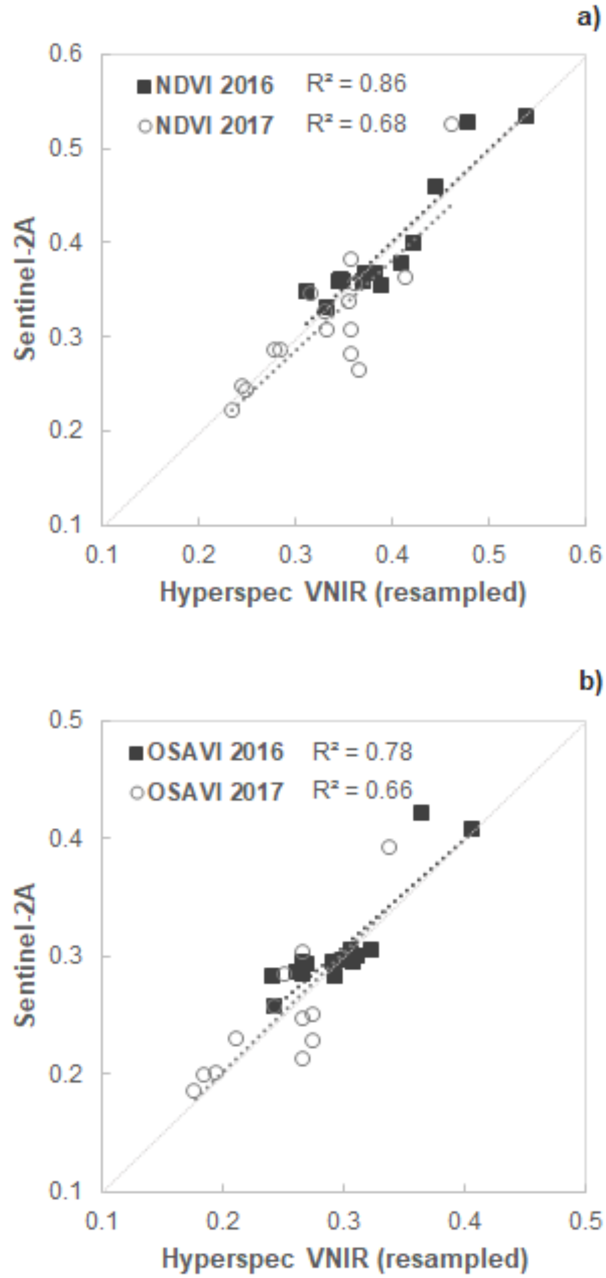

Figure 4. Comparison between Sentinel-2A and high spatial resolution aircraft (Hyperspec VNIR) imagery using the vegetation indices NDVI (top) and OSAVI (bottom) of 16 olive orchards surveyed in June 2016 and July 2017.

2.4. Model simulations

We used a coupled leaf-canopy radiative transfer model to analyse the sensitivity of different VIs to orchard-level changes in *Xf* symptoms through time and to evaluate the effects of the background and soil on the detection of the symptoms. The leaf optical properties were simulated with the PROSPECT-D model (Feret *et al.*, 2017) which requires seven variables: the leaf structure coefficient (N), chlorophyll content (C_{a+b}), carotenoid content (C_{x+c}), anthocyanin content (Anth), brown pigment content (C_{brown}), water equivalent thickness (C_w) and dry matter content (C_m). The PROSPECT leaf model was coupled to the 3-dimensional FLIGHT model (Hernández-Clemente *et al.*, 2017; North, 1996) to simulate the optical effects stemming from heterogeneous architecture of the olive tree crowns and orchards. FLIGHT uses Monte Carlo Ray Tracing (MCRT) techniques for the radiative transfer within crowns and between crowns and other canopy components. FLIGHT calculates directional reflectance of the canopy by accumulating photon energy in the observation direction as a function of different components defining the canopy structure (crown shape and size, tree height, position, density and distribution) (Table 3).

Table 3. Nominal values used in PROSPECT+FLIGHT simulation analysis.

Variable	***Variable code***	***Nominal values***
PROSPECT		
Structure coefficient	N	1.2
Chlorophyll content	C_{a+b} (µg/cm^2)	10 – 80
Carotenoid content	C_{x+c} (µg/cm^2)	10
Anthocyanin content	Anth (µg/cm^2)	1.0
Brown pigment content	C_{brown}	0.0
Water content	C_w (cm)	0.015
Dry matter	C_m (g/cm^2)	0.009
FLIGHT		
Mode of operation	MODE	r (reverse)
Dimension of model	FLAG	3 (3D Representation)
Solar zenith, view zenith (°)	θs, θv	39.27, 0.0
Solar azimuth, view azimuth (°)	Φs, Φv	103.87, 0.0
Number of wavebands	NO_WVBANDS	401
Image size	IM_SIZE	200 x 200
Number of photons traced	-	40000 (reverse mode, from image size)
Total LAI (LAI crown)	TOTAL_LAI	0.25 – 3.5
Leaf angle distribution	LAD [1–9]	0.015, 0.045, 0.074, 0.1,0.123, 0.143, 0.158,0.168, 0.174
Fractional cover (%)	FRAC_COV	5 – 55

Using the described PROSPECT+FLIGHT modelling approach, we generated a look-up table (LUT) to investigate the temporal dynamics of *Xf* incidence using VIs calculated from simulated spectra. We built an LUT with 7056 simulations using the input parameters described in Table 3. The nominal values used to generate the simulations were defined based on field measurements and hyperspectral imagery (Table 3), and mimicked the orchards' architecture and the level of disease impact across the study area. The 40 cm spatial resolution hyperspectral images (Fig. 3 top) were used to distinguish the scene components (Fig. 5), facilitating the parametrisation of the FLIGHT model simulations. In particular, we quantified the fractional cover of each orchard (FCo) using the high-resolution NDVI image obtained from the airborne hyperspectral sensor. To this image, a threshold of NDVI > 0.3 was applied to distinguish tree crowns from background pixels during image segmentation according to the Niblack's thresholding method (Niblack, 1986) and Sauvola's binarisation techniques (Sauvola and Pietikäinen, 2000). Next, we applied a binary watershed analysis using the Euclidean distance map for each object to automatically separate trees with overlapping crowns, which enables to rebuild the scene with the same features. The FCo values retrieved from the airborne sensor were related to the field observations (DSo and DIo) with a linear regression model (r^2=0.67, $p<0.05$) used as a proxy of DSo and DIo in the model simulation. The relationship between FCo and DSo was used to mimic the natural range of variation in FCo values for each DSo and used as input in the LUT. The initial LUT was then classified to set an approximate range of FCo per DSo and DIo (Table 4). For each class (Level 0 to 4), we assumed a range of crown diameters and LAI per orchard to comply with the FCo defined for each level. We also assumed a range of decrease in the chlorophyll content values corresponding to the increase in DSo to mimic the typical discolouration observed in *Xf*-affected olive trees.

Figure 5. Overview of an olive grove acquired with a 40-cm hyperspectral sensor enabling the identification of single trees (left panel) and a 3-D scene generated with FLIGHT Monte Carlo simulation mimicking crowns distribution (right panel).

Table 4. Classification criteria in the model inversion, including disease severity (DSo) and fractional cover (FCo) at orchard level, leaf area index at both crown (LAI_{CROWN}) and scene level (LAI_{SCENE}), and chlorophyll content (C_{a+b})

Level	DSo	FCo	LAI_{CROWN}	C_{a+b}	LAI_{SCENE}
0	Healthy	45 – 55	2 – 3.5	65 – 80	0.9 – 1.925
1	Initial severity	25 – 45	1.5 – 2	50 – 65	0.375 – 0.9
2	Medium severity	20 – 25	0.75 – 1.5	35 – 50	0.15 – 0.375
3	High severity	10 – 20	0.5 – 0.75	20 – 35	0.05 – 0.15
4	Very high severity	5 – 10	0.25 – 0.5	10 – 20	0.0125 – 0.05

To define the synthetic dataset associated with the change, we established a pool of combinations of change describing the positive increase rate of severity ($c = \sum_{k=1}^{5} k$) between orchards classified at different levels for the years *n* and *n+1* (*year* n_{L4}→ *year* $n+1_{L4}$, *year* n_{L3}→ *year* $n+1_{L3}$, *year* n_{L3}→ *year* $n+1_{L4}$, …, *year* n_{L0}→ *year* $n+1_{L4}$). The rate of change between simulations of years *n* and *n+1* was used for the final retrieval of ΔDI and ΔDS.

Three different approaches were considered to account for the canopy background: i) a more complex solution that included the background spectral reflectance variation recorded by the hyperspectral images between 2016 and 2017 for each plot, named as temporal background per plot (TBP); ii) a simpler approach considering a constant spectral reflectance for the background (PB) using a bare-soil spectrum extracted from the hyperspectral imagery collected in 2016; and iii) a compromise solution by computing the average of the background's spectral reflectance recorded for all plots during 2016 and 2017, named as the mean temporal background scheme (MTB). The performance of the model was evaluated based on the Root Mean Square Error (RMSE) between the DI increase estimated from the retrieved Sentinel-2 data and the field observations collected from the 16 orchards.

3. Results

In this section we present the results from the empirical approach to detect variations in DI of *Xf*-affected olive orchards using physiological and structural vegetation indices calculated from Sentinel-2 imagery data. It is followed by the modelling results using a 3-D radiative transfer model to predict temporal changes of *Xf* incidence accounting for the soil and understory variations affecting the temporal trends.

3.1. Temporal trends of DS and DI and vegetation indices

Both the DI and DS caused by *Xf* increased between 2016 and 2017 at all surveyed olive orchards (Fig. 6). DS and DI were significantly correlated with each other (r^2=0.84, $p<0.05$) as were the temporal change rates ΔDS and ΔDI (r^2=0.79, $p<0.05$) (data not shown). Orchards where incidence had already reached 100% continued to see an increase in symptom severity (e.g. A5 and A4), and orchards with a low initial incidence and severity (e.g. C20 to B3), one year later showed a strong increase in both, as reflected by high ΔDI and ΔDS, respectively (e.g. B3).

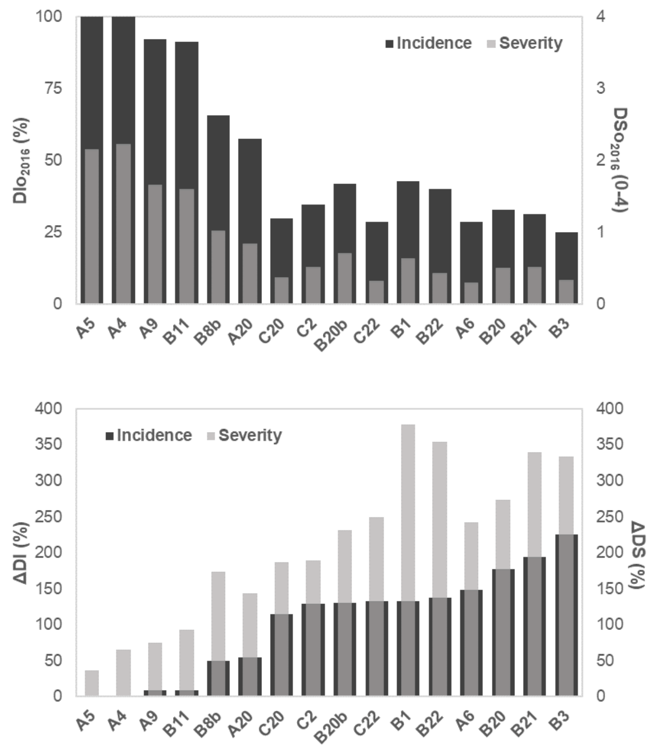

Figure 6. Temporal evolution of DIo and DSo between 2016 and 2017. X-axis labels refer to the 16 olive orchards surveyed.

The rate of change in 17 out of the 25 Sentinel-2 vegetation indices correlated significantly ($p<0.001$) with ΔDS and ΔDI, and six of them showed a coefficient of determination (r^2) exceeding 0.57 (Fig. 7). The indices ARVI and OSAVI produced the highest coefficients of determination with ΔDI (r^2=0.75 and r^2=0.76, respectively; $p<0.001$) (Fig. 8). Classical vegetation indices such as ATSAVI and NDVI yielded similar results (r^2=0.72 and r^2=0.71, respectively), and outperformed RDVI (r^2=0.65) and MSR (r^2=0.61). Relating those VIs to ΔDS generated a similar ranking (r^2_{ARVI}=0.74, r^2_{OSAVI}=0.71, r^2_{ATSAVI}=0.72, r^2_{NDVI}=0.71, r^2_{RDVI}=0.57, r^2_{MSR}=0.6, $p<0.001$). Surprisingly, however, greater ΔDI was associated with smaller reductions in the vegetation indices, whether considering entire orchards (Fig. 8), the background cover only (Fig. 9a), or tree crowns only (Fig. 9b).

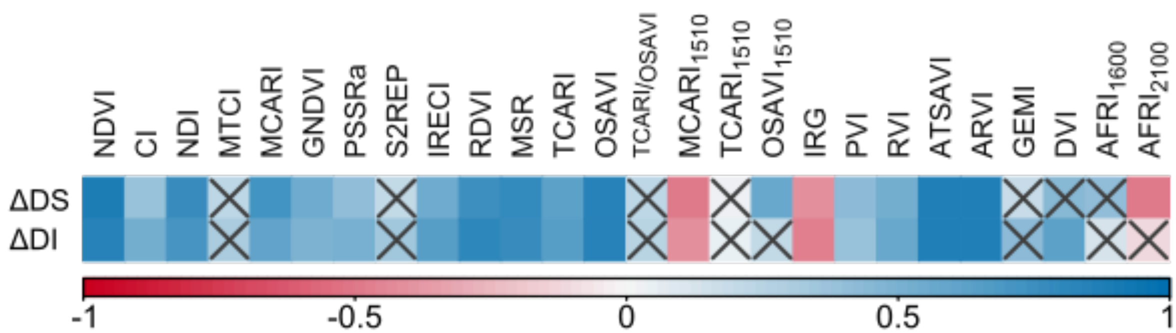

Figure 7. Relationship between severity (ΔDS) and incidence increase (ΔDI) and temporal rate of change in Sentinel-2 vegetation indices selected for this study. Correlation coefficient ranges from -1 to 1. Cross symbols indicate non-significant relationships (p-value ≥ 0.001).

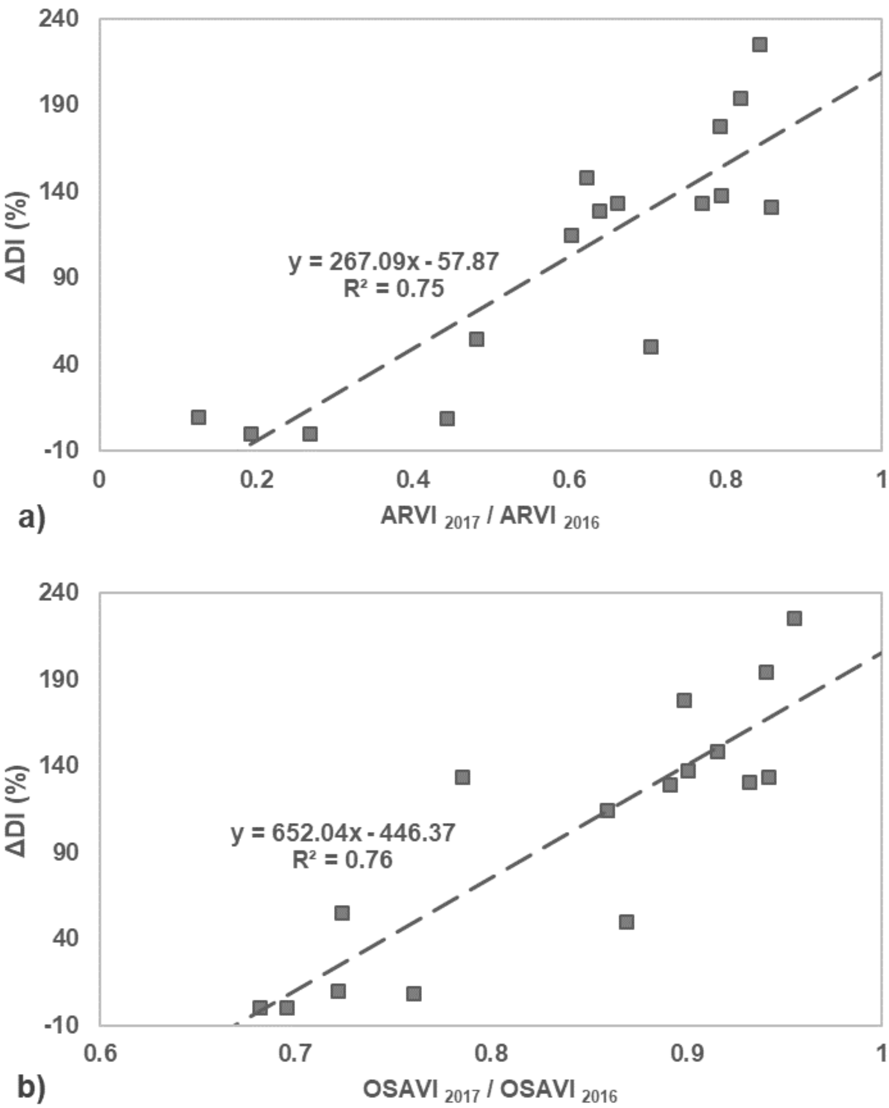

Figure 8. Relationship between *Xf*-incidence increase (ΔDI) and the rate of change of the vegetation indices ARVI (a) and OSAVI (b). Rate of change was calculated from Sentinel-2 images taken in 2016 and 2017.

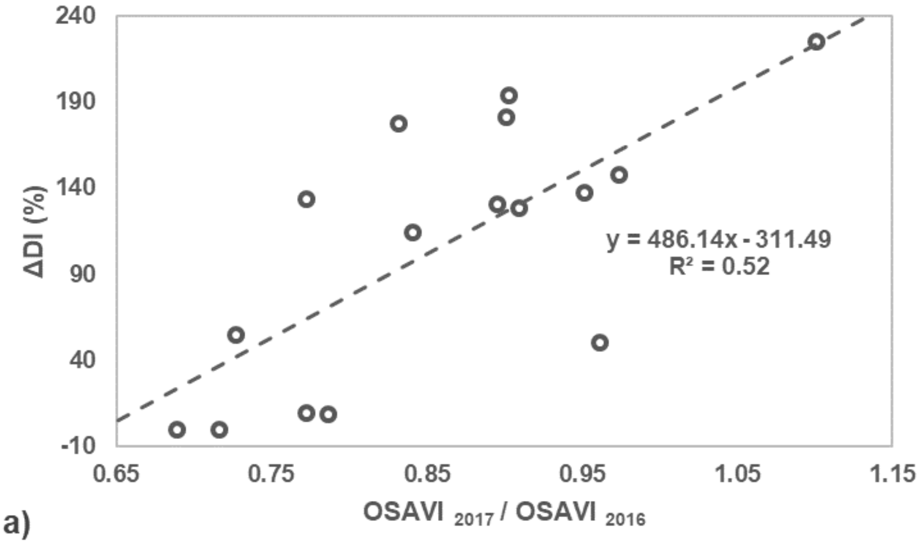

a)

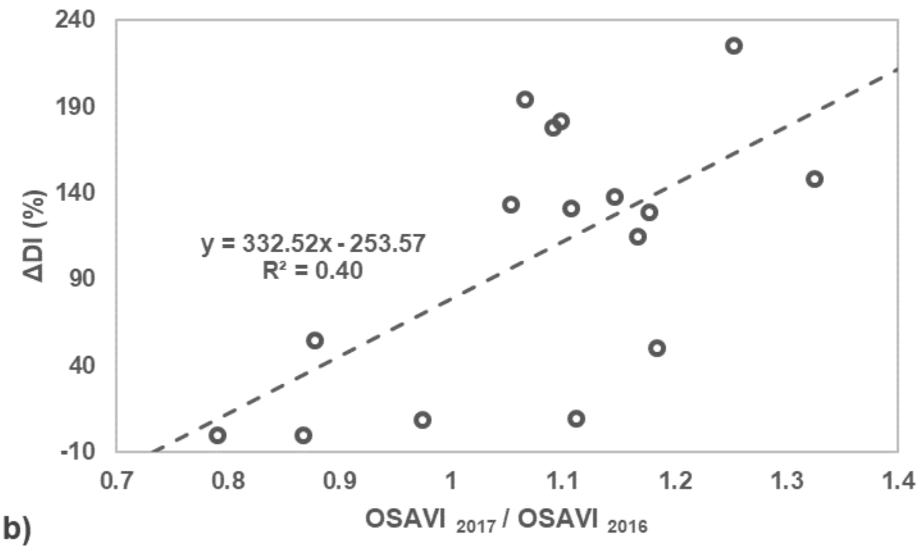

b)

Figure 9. Relationship between *Xf*-incidence increase (ΔDI) and the rate of change of the vegetation index OSAVI with the background around a tree (a), with a radius of 5 metres around its centroid and masking the tree crown itself by segmentation; and taking only tree crowns (b). Rate of change was calculated from hyperspectral imagery in 2016 and 2017 due to its resolution to discriminate between background and trees.

The analysis of the temporal evolution of Sentinel-2A ARVI and OSAVI data revealed distinct patterns in orchards with medium and high DI over the last two years (Fig. 10). Orchards with high DI had a lower ARVI and OSAVI than those with medium DI. The differences were most substantial during the summer. In this season, the VIs tended to be lower than in winter and much less variable than in spring. In addition, a much higher degree of variation was observed during the spring, the season when infection symptoms may develop, and potentially depend on local-scale environmental conditions, as well as the physiological status of individual trees.

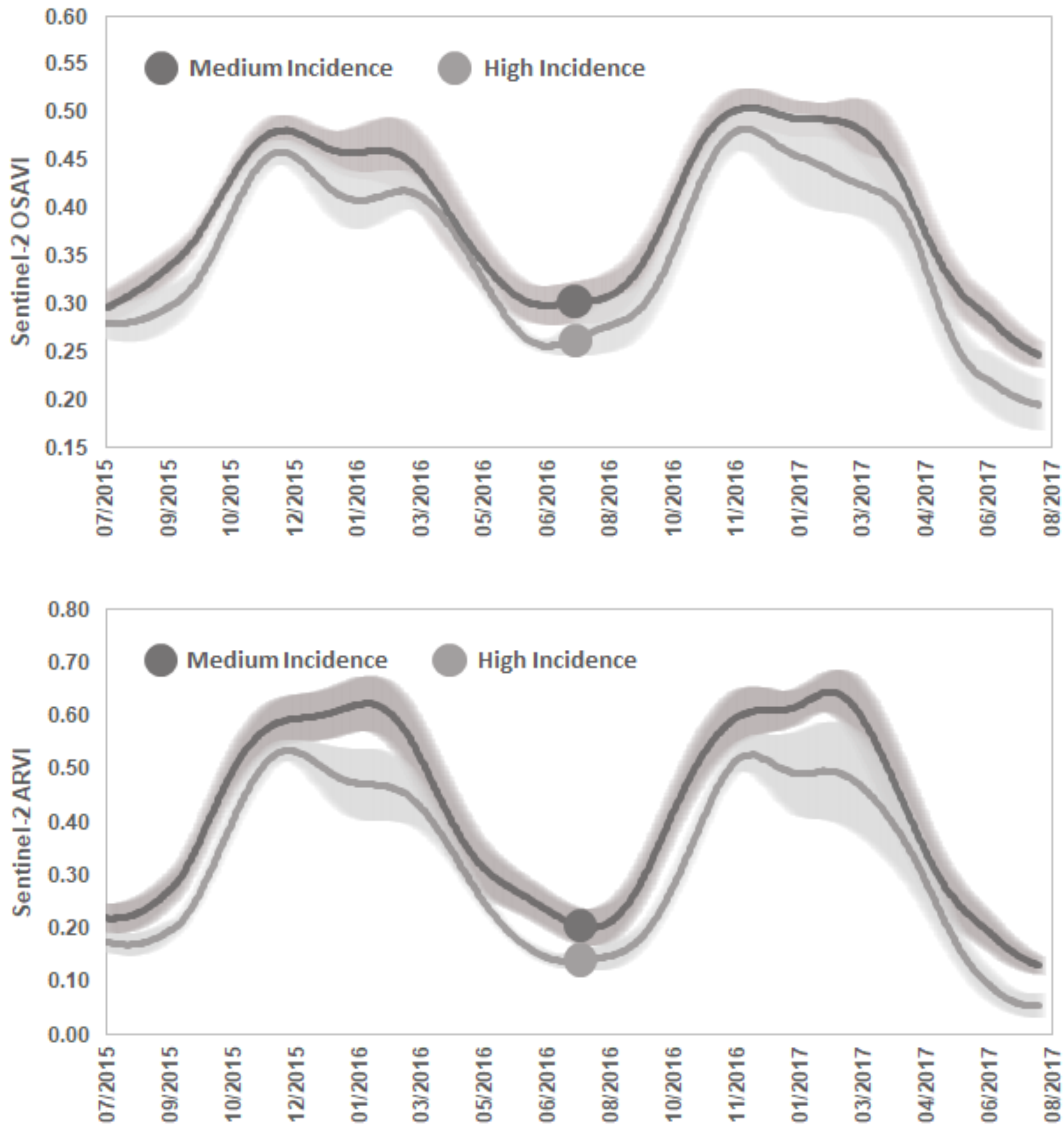

Figure 10. Daily mean OSAVI (top) and ARVI (bottom) time-series of orchards with medium and high *Xf*-incidence as evaluated in the field on 28th June 2016 (dots indicate the timing of the field survey). Lines represent the mean of medium (DIo_{2016}<50%; n=10) and high incidence (DIo_{2016}>50%; n=6) orchards, and bands extend two standard deviations around them.

3.2. Modelling changes in vegetation trends with Sentinel-2

The results of the radiative transfer modelling approach proposed to evaluate the sensitivity of VIs to track the temporal evolution of the disease are displayed in Figure 11. The FLIGHT model simulations obtained using a synthetic multi-temporal dataset of values within the typical range of variation observed in olive groves affected by *Xf* in two consecutive years for OSAVI (Fig. 11a) and ARVI (Fig. 11b) show a direct relationship between ΔDI and the rate of change between two years. The simulated VIs generated using the MTB approach were significantly related to ΔDI for OSAVI, ARVI and NDVI yielding similar accuracy to the empirical relationship with OSAVI (r^2=0.74) but somewhat lower with ARVI (r^2=0.49) and higher for NDVI (r^2=0.68) (data are not shown). In any case, their linear response matched the empirically inferred one very closely.

ΔDI estimated through model inversion using different vegetation indices (ARVI and OSAVI) corresponded well with field observation of the ΔDI temporal change (Fig. 12). The complexity in accounting for the background in the models had an effect on the goodness-of-fit, introducing a bias in the DI change estimates (Fig. 12); when the year-to-year evolution of the background was considered independently for each of the orchards (TBP approach), the model simulations were entirely corrected for background effects and, therefore, the accuracy of ΔDI retrievals using OSAVI and ARVI was significantly higher ($RMSE_{OSAVI}$=43% and $RMSE_{ARVI}$=44%) (Fig. 12 a, b). Model performance decreased when instead the mean background reflectance time-series from all orchards (MTB approach) was used as model input ($RMSE_{OSAVI}$=50% and $RMSE_{ARVI}$=84%, Fig. 12 c, d). Finally, when model simulations did not account for the temporal changes in background reflectance at all (PB approach), the fitted models degraded significantly, leading to larger errors (*RMSE*≥140%) (Fig. 12 e, f).

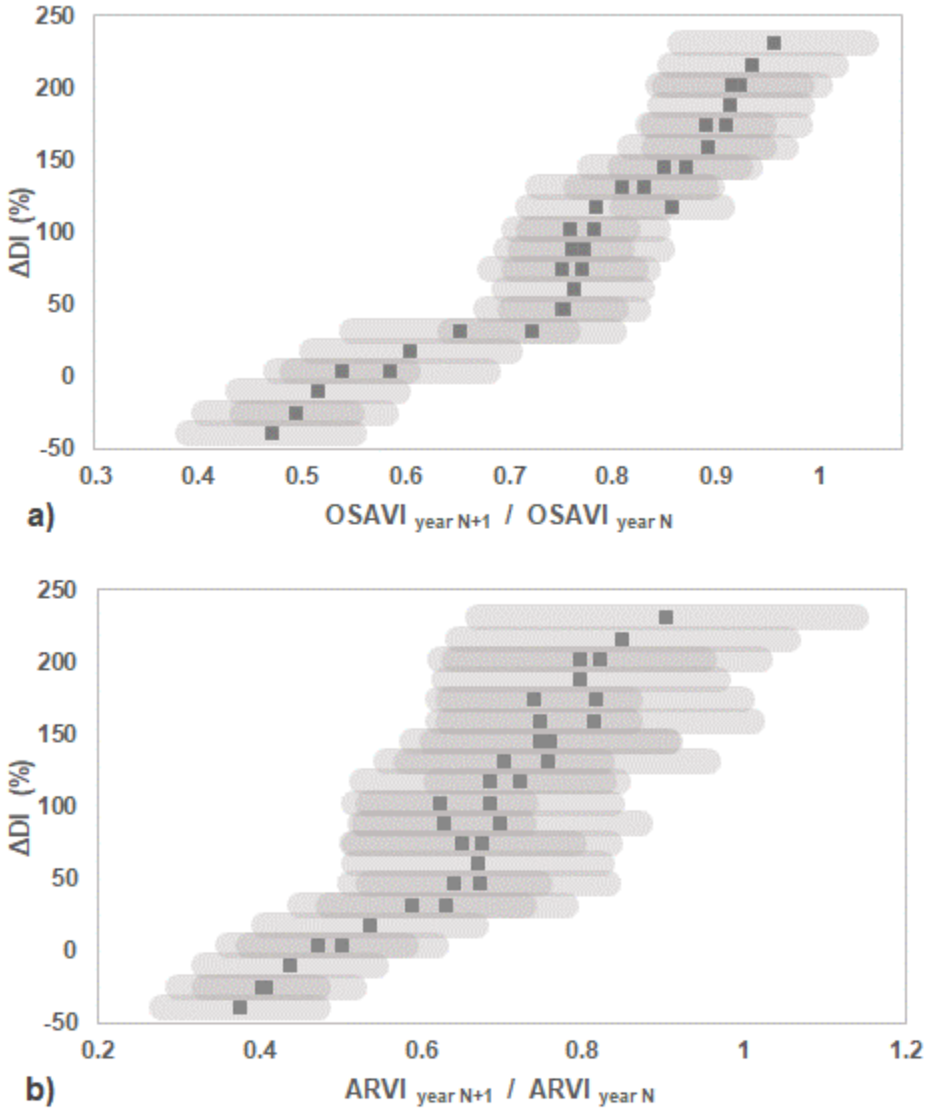

Figure 11. Simulations of the disease incidence increase (ΔDI) with OSAVI (a) and ARVI (b), generated by PROSPECT+FLIGHT and using the average spectral reflectance measured in parts of the orchards not covered by olive tree crowns to represent the background in the model (MTB approach).

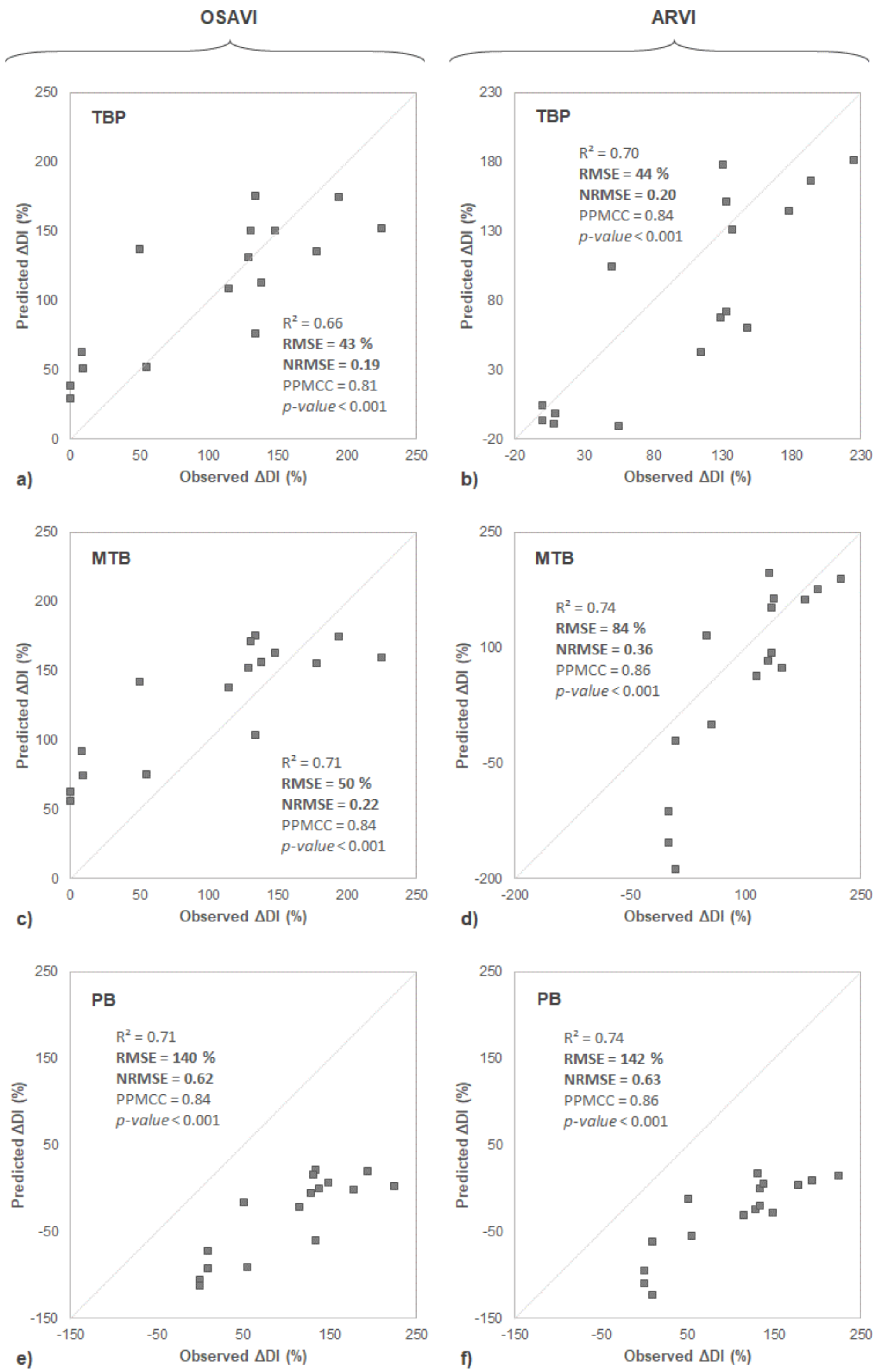

Figure 12. Estimated versus measured *Xf*-increase incidence (ΔDI) using OSAVI (left) and ARVI (right) vegetation indices. PROSPECT+FLIGHT inversions calculated using TBP (a, b), MTB (c, d) and PB (e, f).

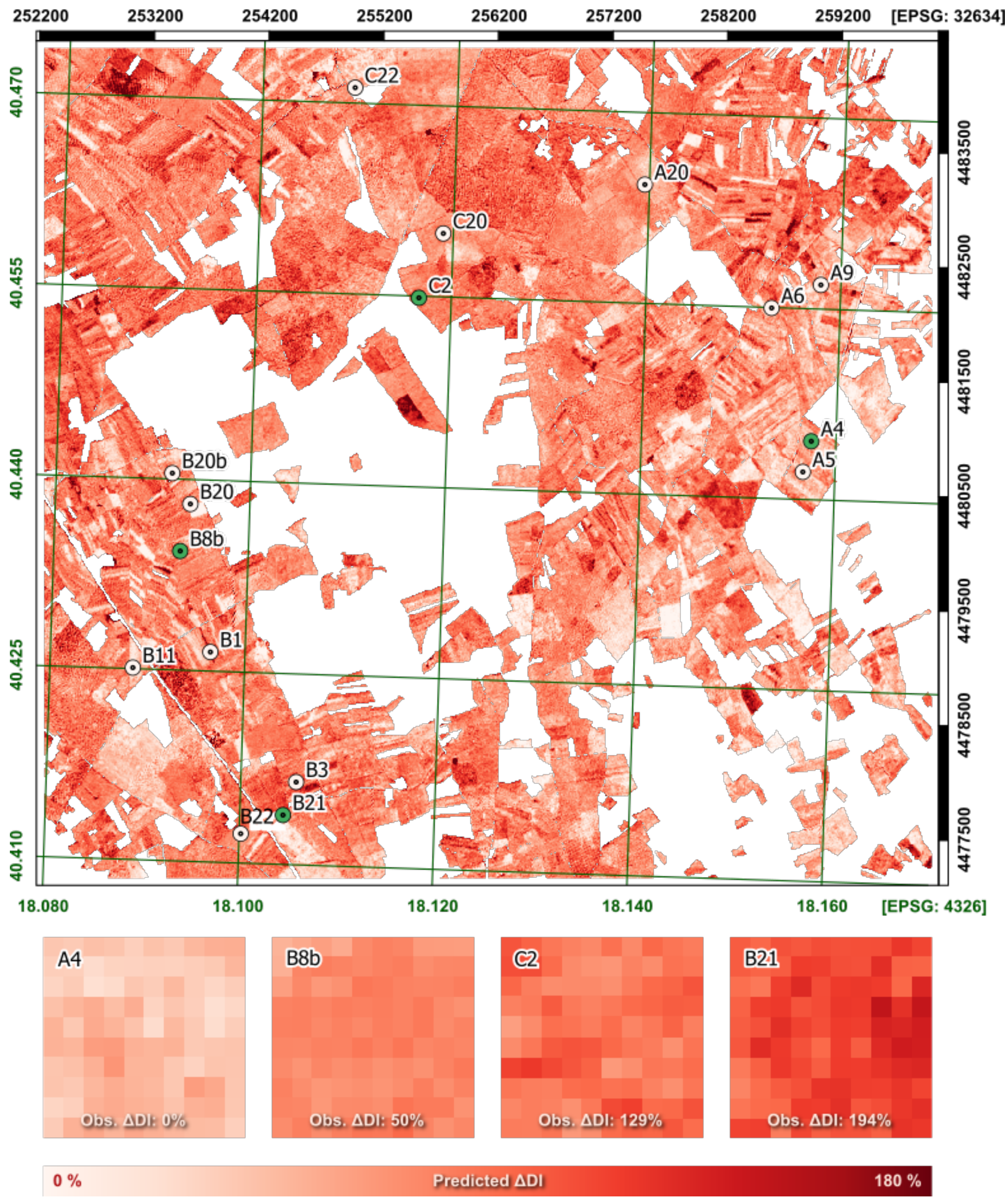

Figure 13. *Xf*-disease incidence increase (ΔDI) map generated from Sentinel-2A data of 29th June 2016 and 24th June 2017 using a lookup-table generated by inverting a PROSPECT+FLIGHT model that considered the temporal changes in background reflectance (MTB approach, see text for details). Dots in the map indicate the individual olive orchards that were surveyed in the field. Bottom panels show incidence increases over different areas (green dots) where olive orchards were surveyed. Observed incidence increase for each selected orchard is also indicated. The map has been masked with a layer of olive groves for Puglia extracted from the Puglia Land Cover 2011 (InnovaPuglia Spa - Servizio Territorio e Ambiente, 2013).

Applying this methodology with OSAVI and the MTB model (Fig. 11 a, Fig. 12 c) to entire Sentinel-2A scenes generated a map of the predicted increase in *Xf*-symptom incidence between 29th June 2016 and 24th June 2017 (Fig. 13).

4. Discussion

The first research question of this study was to analyse if satellite data could be used to monitor temporal changes of *Xf*-induced DI and DS, and provide insights into the epidemiology of *Xf* spread over large areas. Previous work showed that non-visual symptoms of *Xf* infection can be detected with very high-resolution hyperspectral images and radiative transfer models (Zarco-Tejada *et al.*, 2018a), providing an innovative tool for the early detection of infected olive trees at local scales. However, since *Xf* has spread rapidly iin Southern Italy in the last years affecting entire olive orchards, tracking more conspicuous damage (such as DI and DS) across large areas could help measure, forecast, and mitigate the impact of *Xf* on the landscape, and on socio-economic sectors depending on it (Luvisi *et al.*, 2017; White *et al.*, 2017). The fast spread is reflected in our field observations: DI and DS increased considerably between 2016 and 2017, and ΔDI and ΔDS were linearly related. Indeed, the widespread increase of Xf infections in the last three years in southern Apulia (Girelli *et al.*, 2017) has posed a risk to the olive trees and sector in the region.

In natural conditions, biotic and abiotic factors jointly affect the development of vegetation diseases over different spatial and temporal scales. The interaction may cause a progressive loss in chlorophyll and biomass producing irreversible changes in the vegetation. Both alterations are detectable and quantifiable through VIs calculated from Sentinel-2 data (Zarco-Tejada *et al.*, 2019). However, relationships between VIs (OSAVI or NDVI) and DS or DI were poor when considering data from 2016 and 2017 together ($r2<0.22$, $p<0.05$) (Fig. 1, supplementary material), indicating that the VIs reflect other orchard characteristics than *Xf*-symptoms and that these characteristics vary considerably between years. Hence, a precise disease assessment requires a quantitative estimation of the temporal evolution of the disease (ΔDI and ΔDS) rather than a mere quantification of DI and DS at one specific time (Nutter *et al.*, 2006). Indeed, the availability of frequent multispectral data from Sentinel-2 offers the opportunity to assess, not only spatial, but also temporal variation in VIs to monitor *Xf* infections in olive orchards over time.

When working with multi-temporal data acquired over non-closed canopies, one of the main challenges is to decouple the spectral reflectance changes produced by alterations in the vegetation condition from those produced by atmospheric and background factors. Here, the seasonal variation of VIs showed thighest variability in winter and early spring. In these periods, cloudy days are more frequent, increasing the residual noise in the data and the need for temporal interpolation. The sensitivity of different vegetation indices to soil background and atmospheric effects were previously analysed by in efforts to improve the accuracy of the retrieval of LAI and absorbed photosynthetically active radiation (APAR) (Baret and Guyot, 1991b; Haboudane *et al.*, 2004; Huete *et al.*, 1985) and chlorophyll (Haboudane *et al.*, 2008; Zhang *et al.*, 2008). The variation in FC of forest under decline also affects the performance of some vegetation indices with higher sensitivity to canopy structure changes (Hernández-Clemente *et al.*, 2011). The best-performing VIs in our study, OSAVI and ARVI, tend to be relatively robust to background and atmospheric effects (Kaufman and Tanre, 1992b; Rondeaux *et al.*, 1996). Empirical and modelling results agreed regarding the accuracy of OSAVI as the best-performing index to track ΔDI. In contrast, the sensitivity of ARVI to the field observations was not entirely confirmed by model simulations. This may be related to the fact that ARVI is a vegetation index that minimises the atmospherical effects on the reflectance, conditions that were not included in the modelling which assumed stable atmospherical conditions for both years.

In either case, the overall robustness shown by modified VIs such as OSAVI or ARVI is in disagreement with some other studies where traditional indices had a better performance. For instance, Frampton *et al.* (2013) found that LAI and chlorophyll could be extracted from Sentinel-2 NDVI images for crops as well as from novel indices such as S2REP and MTCI. Differences in the homogeneity of crops versus olive orchard canopies might explain this apparent contradiction; in the latter case, the confounding effects produced by the structural heterogeneity of the orchards invalidates VIs with high sensitivity to soil effects and atmospheric conditions.

The contribution of the background seems to affect not only the spectral reflectance of the canopy measured by Sentinel-2 but also the spectral reflectance retrieved from the diseased crowns using hyperspectral images. Both sensors, with different spatial and spectral resolutions, namely showed a significant and similar relationship with greater ΔDI leading to greater VI increases. This counterintuitive result is unlikely to be driven by weather patterns in the two years, as the sampled orchards experience very similar meteorological conditions. Instead it might reflect the impact that the background has on the crown spectral response as olive trees crowns generally have low transmittance and LAI (Gómez Calero *et al.*, 2011) and defoliation increased with DS. As a result, the background has a particularly large contribution to the temporal VI trends once *Xf* disease symptoms are severe, even when using self-corrected (Kaufman and Tanre, 1992b) and soil-adjusted (Rondeaux *et al.*, 1996) VIs and considering only tree crowns. Simultaneously, the increase in *Xf* infections was associated with a decrease in FC of the trees and an increase in the FC of the background, further increasing the dominance of the understory in the signal at orchard resolution. The inverse effect of an increase in the greenness of the background when the health of *Xf*-infected trees decreases could be management driven if diseased orchards are abandoned, and no longer mowed or ploughed, leaving low-stature vegetation to reoccupy the soil. It may also be partly ecologically driven if diseased trees leave more nutrients and water available to the understory (Peltzer and Köchy, 2001).

This pattern further emphasises the relevance of incorporating 3-D radiative transfer models (RTMs) when analysing VIs to explicitly incorporate background effects if the impact of *Xf* on spectral characteristics of olive groves is to be modelled with considerable precision (Meggio *et al.*, 2008; Richardson and Wiegand, 1977). This drove us to answer our second research question showing the feasibility of modelling changes in DI from multi-temporal Sentinel-2 image data using different vegetation indices and radiative transfer models. In fact, the background effect has a significant impact on the model estimation against in-situ measurements; there was an improvement in the retrieval of ΔDI of 33.5% when accounting for the background effects, and a further 9.5% when its heterogeneity was also considered. These results have critical implications in the use of vegetation indices to assess the temporal evolution of the disease due to the non-homogeneous background effects across orchards affected by *Xf* altering the spectral signature of the canopy with Sentinel-2 image data. The simulation approach demonstrated the benefit of using a 3-D radiative transfer model accounting for those effects, which is critical to monitoring future spread of *Xf* infections and understanding its epidemiology (Fuente *et al.*, 2018). Therefore, this study takes one step further via modelling methods for change monitoring, enabling the retrieval of vegetation trends associated with *Xf* infections and improving the understanding of the dynamics of the understory.

The methodology proposed based on the use of RTM and Sentinel-2 imagery offers the advantage of using free satellite data in comparison to any other remote sensing product limited by the availability of hyperspectral images. However, the applicability of these methods into a systematic detection system may be limited by the computational time required through model inversion, notwithstanding this limitation can be overcome in combination with data-driven machine learning algorithmsbased on multi-output algorithms emulating the functioning of RTM (Rivera *et al.*, 2015). The result of mapping disease-incidence dynamics using radiative transfer modelling illustrates the potential of the medium-spatial resolution Sentinel-2 sensor to assess olive groves' health dynamics. The challenge of mapping disease infections has been thus far mainly addressed using environmental data and probabilistic models (Hay *et al.*, 2006) and rarely met in quantitative terms. Remote sensing combining radiative transfer and vegetation indices makes it possible to map *Xf*'s DI dynamics based on the main biophysical changes *Xf* causes not only in plants, but in the entire landscape. The dense time-series, which the Sentinel-2 satellites now provide, possibly in combination with Landsat, means such mapping could, in theory, be carried out on a near-monthly basis bringing new opportunities for monitoring *Xf* disease incidence over large areas. Future work towards this aim should particularly consider how to disentangle direct plant-level effects of *Xf* infection from those that manifest themselves in other components of the landscape, either because of changes in vegetation composition or management.

5. Conclusions

This study demonstrates that Sentinel-2 enables the detection of changes associated with temporal variations of *Xf*-induced symptoms at the orchard level. The work used a two-year dataset, integrating Sentinel-2 satellite images and high-resolution hyperspectral imagery, field observations and radiative transfer modelling. The temporal rate of change of disease incidence (DI) and severity (DS) was evaluated using different VIs showing that the monitoring of *Xf*-infected orchards required the use of self-corrected and soil-adjusted VIs. Among all the Sentinel-2 VIs studied, the best performance was found for those that minimised the atmospheric and background effects such as ARVI, OSAVI and ATSAVI. These VIs performed better than traditional vegetation indices when used as a quantitative proxy of the fractional cover (FC) of green and healthy vegetation, such as NDVI, RDVI and MSR. However, the confounding effects of the understory had a considerable impact on the VIs calculated from Sentinel-2 over infected olive orchards due to the discontinuous canopies characteristic of this crop. Therefore, this study demonstrated that 3-D RTM and field observations properly explained the temporal variations in both tree canopy and background, required to accurately predict ΔDI and ΔDS. Applying a temporal trend analysis supported by the 3-D RTM demonstrated that ARVI and OSAVI can be used to monitor orchard-level changes in DI and DS, yielding Normalised Root Mean Square Error (NRMSE) values below 0.22 and 0.36 respectively for the two years of analysis. Overall, these results suggest that Sentinel-2 time-series data can provide useful spatio-temporal indicators to monitor the damage caused by *Xf* infections across large areas.

Acknowledgements

Data collection was partially supported by the European Union's Horizon 2020 research and innovation programme through grant agreements POnTE (635646) and XF-ACTORS (727987). A. Hornero was supported by research fellowship DTC GEO 29 "Detection of global photosynthesis and forest health from space" from the Science Doctoral Training Centre

(Swansea University, UK). The authors would also like to thank QuantaLab-IAS-CSIC (Spain) for laboratory assistance and the support provided during the airborne campaigns and the image processing. B. Landa, C. Camino, M. Montes-Borrego, M. Morelli, M. Saponari and L. Susca are acknowledged for their support during the field campaigns, as well as IPSP-CNR and Dipartimento di Scienze del Suolo (Università di Bari, Italy) as host institutions. The views expressed are purely those of the writers and may not in any circumstance be regarded as stating an official position of the European Commission.

All the figures included in this manuscript have been designed by taking into account colour schemes prepared for people with visual disabilities and considering that they can be printed correctly (Harrower and Brewer, 2003).

Appendix A. Supplementary material

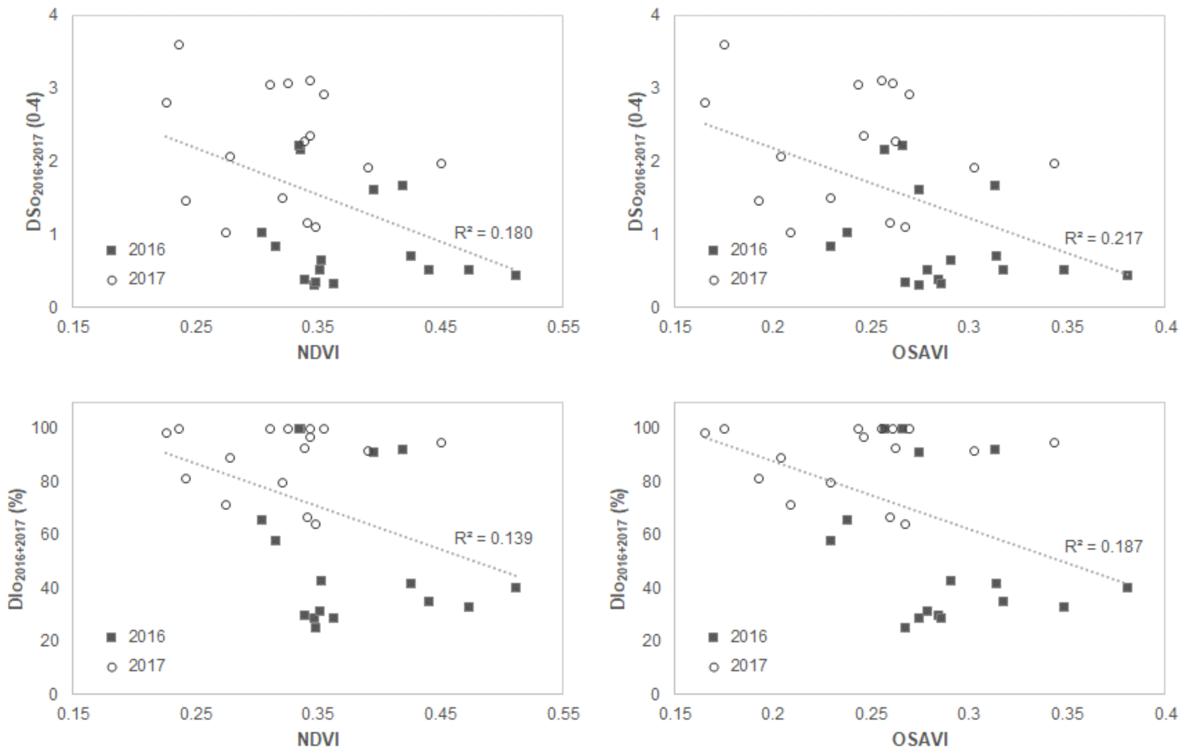

Figure 1. *Supplementary material*. Relationship between severity (DSo) and incidence (DIo) and VIs calculated from Sentinel-2A imagery in 2016 and 2017.

References

Almeida, R.P.P., Nunney, L., 2015. How Do Plant Diseases Caused by Xylella fastidiosa Emerge? Plant Disease 99, 1457–1467. https://doi.org/10.1094/PDIS-02-15-0159-FE

Araya-López, R.A., Lopatin, J., Fassnacht, F.E., Hernández, H.J., 2018. Monitoring Andean high altitude wetlands in central Chile with seasonal optical data: A comparison between Worldview-2 and Sentinel-2 imagery. ISPRS Journal of Photogrammetry and Remote Sensing. https://doi.org/10.1016/j.isprsjprs.2018.04.001

Assal, T.J., Anderson, P.J., Sibold, J., 2016. Spatial and temporal trends of drought effects in a heterogeneous semi-arid forest ecosystem. Forest Ecology and Management 365, 137–151. https://doi.org/10.1016/j.foreco.2016.01.017

Atzberger, C., Richter, K., 2012. Spatially constrained inversion of radiative transfer models for improved LAI mapping from future Sentinel-2 imagery. Remote Sensing of Environment, The Sentinel Missions - New Opportunities for Science 120, 208–218. https://doi.org/10.1016/j.rse.2011.10.035

Bannari, A., Morin, D., Bonn, F., Huete, A.R., 1995. A review of vegetation indices. Remote Sensing Reviews 13, 95–120. https://doi.org/10.1080/02757259509532298

Baret, F., Guyot, G., 1991a. Potentials and limits of vegetation indices for LAI and APAR assessment. Remote Sensing of Environment 35, 161–173. https://doi.org/10.1016/0034-4257(91)90009-U

Baret, F., Guyot, G., 1991b. Potentials and limits of vegetation indices for LAI and APAR assessment. Remote Sensing of Environment 35, 161–173. https://doi.org/10.1016/0034-4257(91)90009-U

Bayat, B., Van der Tol, C., Verhoef, W., 2016. Remote Sensing of Grass Response to Drought Stress Using Spectroscopic Techniques and Canopy Reflectance Model Inversion. Remote Sensing 8, 557. https://doi.org/10.3390/rs8070557

Beck, P.S.A., Juday, G.P., Alix, C., Barber, V.A., Winslow, S.E., Sousa, E.E., Heiser, P., Herriges, J.D., Goetz, S.J., 2011. Changes in forest productivity across Alaska consistent with biome shift. Ecology Letters 14, 373–379. https://doi.org/10.1111/j.1461-0248.2011.01598.x

Blackburn, G.A., 1998. Spectral indices for estimating photosynthetic pigment concentrations: A test using senescent tree leaves. International Journal of Remote Sensing 19, 657–675. https://doi.org/10.1080/014311698215919

Brilli, L., Chiesi, M., Maselli, F., Moriondo, M., Gioli, B., Toscano, P., Zaldei, A., Bindi, M., 2013. Simulation of olive grove gross primary production by the combination of ground and multi-sensor satellite data. International Journal of Applied Earth Observation and Geoinformation 23, 29–36. https://doi.org/10.1016/j.jag.2012.11.006

Bye, I.J., North, P.R.J., Los, S.O., Kljun, N., Rosette, J.A.B., Hopkinson, C., Chasmer, L., Mahoney, C., 2017. Estimating forest canopy parameters from satellite waveform LiDAR by inversion of the FLIGHT three-dimensional radiative transfer model. Remote Sensing of Environment 188, 177–189. https://doi.org/10.1016/j.rse.2016.10.048

Castillo, J.A.A., Apan, A.A., Maraseni, T.N., Salmo, S.G., 2017. Estimation and mapping of above-ground biomass of mangrove forests and their replacement land uses in the Philippines using Sentinel imagery. ISPRS Journal of Photogrammetry and Remote Sensing 134, 70–85. https://doi.org/10.1016/j.isprsjprs.2017.10.016

Chen, J.M., 1996. Evaluation of Vegetation Indices and a Modified Simple Ratio for Boreal Applications. Canadian Journal of Remote Sensing 22, 229–242. https://doi.org/10.1080/07038992.1996.10855178

Cleveland, W.S., Grosse, E., Shyu, W.M., 1992. Local regression models. Statistical models in S 2, 309–376.

Commission Implementing Decision (EU) 2018/927 of 27 June 2018 amending Implementing Decision (EU) 2015/789 as regards measures to prevent the introduction into and the spread within the Union of Xylella fastidiosa (Wells et al.) (notified under document C(2018) 3972), 2018. , OJ L.

Dash, J., Curran, P.J., 2007. Evaluation of the MERIS terrestrial chlorophyll index (MTCI). Advances in Space Research 39, 100–104. https://doi.org/10.1016/j.asr.2006.02.034

Delegido, J., Verrelst, J., Alonso, L., Moreno, J., 2011. Evaluation of Sentinel-2 Red-Edge Bands for Empirical Estimation of Green LAI and Chlorophyll Content. Sensors 11, 7063–7081. https://doi.org/10.3390/s110707063

EFSA, 2018. Updated pest categorisation of Xylella fastidiosa. EFSA Journal 16, e05357. https://doi.org/10.2903/j.efsa.2018.5357

Fang, X., Zhu, Q., Ren, L., Chen, H., Wang, K., Peng, C., 2018. Large-scale detection of vegetation dynamics and their potential drivers using MODIS images and BFAST: A case study in Quebec, Canada. Remote Sensing of Environment 206, 391–402. https://doi.org/10.1016/j.rse.2017.11.017

Feret, J.-B., Gitelson, A., Noble, S.D., Jacquemoud, S., 2017. PROSPECT-D: Towards modeling leaf optical properties through a complete lifecycle. Remote Sensing of Environment 193, 204–215. https://doi.org/10.1016/j.rse.2017.03.004

Forkuor, G., Dimobe, K., Serme, I., Tondoh, J.E., 2018. Landsat-8 vs. Sentinel-2: examining the added value of sentinel-2's red-edge bands to land-use and land-cover mapping in Burkina Faso. GIScience & Remote Sensing 55, 331–354. https://doi.org/10.1080/15481603.2017.1370169

Frampton, William James, Dash, J., Watmough, G., Milton, E.J., 2013. Evaluating the capabilities of Sentinel-2 for quantitative estimation of biophysical variables in vegetation. ISPRS Journal of Photogrammetry and Remote Sensing 82, 83–92. https://doi.org/10.1016/j.isprsjprs.2013.04.007

Frampton, W. J., Dash, J., Watmough, G.R., Milton, E.J., 2013. Evaluating the capabilities of Sentinel-2 for quantitative estimation of biophysical variables in vegetation. ISPRS Journal of Photogrammetry and Remote Sensing 82, 83–92. https://doi.org/Frampton, W.J., Dash, J., Watmough, Gary R. and Milton, E.J. (2013) Evaluating the capabilities of Sentinel-2 for quantitative estimation of biophysical variables in vegetation ISPRS Journal of Photogrammetry and Remote Sensing, 82, pp. 83-92. (doi:10.1016/j.isprsjprs.2013.04.007 <http://dx.doi.org/10.1016/j.isprsjprs.2013.04.007>).

Fuente, B. de la, Saura, S., Beck, P.S.A., 2018. Predicting the spread of an invasive tree pest: The pine wood nematode in Southern Europe. Journal of Applied Ecology 55, 2374–2385. https://doi.org/10.1111/1365-2664.13177

Gamon, J.A., Surfus, J.S., 1999. Assessing leaf pigment content and activity with a reflectometer. New Phytologist 143, 105–117. https://doi.org/10.1046/j.1469-8137.1999.00424.x

Gastellu-Etchegorry, J.P., Demarez, V., Pinel, V., Zagolski, F., 1996. Modeling radiative transfer in heterogeneous 3-D vegetation canopies. Remote Sensing of Environment 58, 131–156. https://doi.org/10.1016/0034-4257(95)00253-7

Gillespie, T.W., Ostermann-Kelm, S., Dong, C., Willis, K.S., Okin, G.S., MacDonald, G.M., 2018. Monitoring changes of NDVI in protected areas of southern California. Ecological Indicators 88, 485–494. https://doi.org/10.1016/j.ecolind.2018.01.031

Girelli, C.R., Coco, L.D., Scortichini, M., Petriccione, M., Zampella, L., Mastrobuoni, F., Cesari, G., Bertaccini, A., D'Amico, G., Contaldo, N., Migoni, D., Fanizzi, F.P., 2017. Xylella fastidiosa and olive quick decline syndrome (CoDiRO) in Salento (southern Italy): a chemometric 1H NMR-based preliminary study on Ogliarola salentina and Cellina di Nardò cultivars. Chem. Biol. Technol. Agric. 4, 25. https://doi.org/10.1186/s40538-017-0107-7

Gitelson, A.A., Kaufman, Y.J., Merzlyak, M.N., 1996. Use of a green channel in remote sensing of global vegetation from EOS-MODIS. Remote Sensing of Environment 58, 289–298. https://doi.org/10.1016/S0034-4257(96)00072-7

Gómez Calero, J.A., Zarco-Tejada, P.J., García-Morillo, J., Gama, J., Soriano, M.A., 2011. Determining biophysical parameters for olive trees using CASI-airborne and QuickBird-satellite imagery. https://doi.org/10.2134/agronj2010.0449

Gueymard, C., 1995. SMARTS2: a simple model of the atmospheric radiative transfer of sunshine: algorithms and performance assessment. Florida Solar Energy Center Cocoa, FL.

Gueymard, C.A., 2001. Parameterized transmittance model for direct beam and circumsolar spectral irradiance. Solar Energy 71, 325–346. https://doi.org/10.1016/S0038-092X(01)00054-8

Haboudane, D., Miller, J.R., Pattey, E., Zarco-Tejada, P.J., Strachan, I.B., 2004. Hyperspectral vegetation indices and novel algorithms for predicting green LAI of crop canopies:

Modeling and validation in the context of precision agriculture. Remote Sensing of Environment 90, 337–352. https://doi.org/10.1016/j.rse.2003.12.013

Haboudane, D., Miller, J.R., Tremblay, N., Zarco-Tejada, P.J., Dextraze, L., 2002. Integrated narrow-band vegetation indices for prediction of crop chlorophyll content for application to precision agriculture. Remote Sensing of Environment 81, 416–426. https://doi.org/10.1016/S0034-4257(02)00018-4

Haboudane, D., Tremblay, N., Miller, J.R., Vigneault, P., 2008. Remote Estimation of Crop Chlorophyll Content Using Spectral Indices Derived From Hyperspectral Data. IEEE Transactions on Geoscience and Remote Sensing 46, 423–437. https://doi.org/10.1109/TGRS.2007.904836

Harrower, M., Brewer, C.A., 2003. ColorBrewer. org: an online tool for selecting colour schemes for maps. The Cartographic Journal 40, 27–37.

Hay, S.I., Tatem, A.J., Graham, A.J., Goetz, S.J., Rogers, D.J., 2006. Global environmental data for mapping infectious disease distribution. Adv. Parasitol. 62, 37–77. https://doi.org/10.1016/S0065-308X(05)62002-7

Haynes, W., 2013. Bonferroni Correction, in: Encyclopedia of Systems Biology. Springer, New York, NY, pp. 154–154. https://doi.org/10.1007/978-1-4419-9863-7_1213

Hernández-Clemente, R., Navarro-Cerrillo, R.M., Ramírez, F.J.R., Hornero, A., Zarco-Tejada, P.J., 2014. A Novel Methodology to Estimate Single-Tree Biophysical Parameters from 3D Digital Imagery Compared to Aerial Laser Scanner Data. Remote Sensing 6, 11627–11648. https://doi.org/10.3390/rs61111627

Hernández-Clemente, R., Navarro-Cerrillo, R.M., Suárez, L., Morales, F., Zarco-Tejada, P.J., 2011. Assessing structural effects on PRI for stress detection in conifer forests. Remote Sensing of Environment 115, 2360–2375. https://doi.org/10.1016/j.rse.2011.04.036

Hernández-Clemente, R., Navarro-Cerrillo, R.M., Zarco-Tejada, P.J., 2012. Carotenoid content estimation in a heterogeneous conifer forest using narrow-band indices and PROSPECT+DART simulations. Remote Sensing of Environment 127, 298–315. https://doi.org/10.1016/j.rse.2012.09.014

Hernández-Clemente, R., North, P.R.J., Hornero, A., Zarco-Tejada, P.J., 2017. Assessing the effects of forest health on sun-induced chlorophyll fluorescence using the FluorFLIGHT 3-D radiative transfer model to account for forest structure. Remote Sensing of Environment 193, 165–179. https://doi.org/10.1016/j.rse.2017.02.012

Herrmann, I., Karnieli, A., Bonfil, D.J., Cohen, Y., Alchanatis, V., 2010. SWIR-based spectral indices for assessing nitrogen content in potato fields. International Journal of Remote Sensing 31, 5127–5143. https://doi.org/10.1080/01431160903283892

Herrmann, I., Pimstein, A., Karnieli, A., Cohen, Y., Alchanatis, V., Bonfil, D.J., 2011. LAI assessment of wheat and potato crops by VENμS and Sentinel-2 bands. Remote Sensing of Environment 115, 2141–2151. https://doi.org/10.1016/j.rse.2011.04.018

Hill, M.J., 2013. Vegetation index suites as indicators of vegetation state in grassland and savanna: An analysis with simulated SENTINEL 2 data for a North American transect. Remote Sensing of Environment 137, 94–111. https://doi.org/10.1016/j.rse.2013.06.004

Horsfall, J.G., Cowling, E.B., 1978. Pathometry: the measurement of plant disease. Plant Disease: an Advanced Treatise.

Huete, A., Justice, C., Liu, H., 1994. Development of vegetation and soil indices for MODIS-EOS. Remote Sensing of Environment 49, 224–234. https://doi.org/10.1016/0034-4257(94)90018-3

Huete, A.R., 1988. A soil-adjusted vegetation index (SAVI). Remote Sensing of Environment 25, 295–309. https://doi.org/10.1016/0034-4257(88)90106-X

Huete, A.R., Jackson, R.D., Post, D.F., 1985. Spectral response of a plant canopy with different soil backgrounds. Remote Sensing of Environment 17, 37–53. https://doi.org/10.1016/0034-4257(85)90111-7

InnovaPuglia Spa - Servizio Territorio e Ambiente, 2013. Uso del Suolo [WWW Document]. URL http://www.dataset.puglia.it/dataset/uso-del-suolo-2011-uds (accessed 9.2.18).

Karnieli, A., Kaufman, Y.J., Remer, L., Wald, A., 2001. AFRI — aerosol free vegetation index. Remote Sensing of Environment 77, 10–21. https://doi.org/10.1016/S0034-4257(01)00190-0

Kaufman, Y.J., Tanre, D., 1992a. Atmospherically resistant vegetation index (ARVI) for EOS-MODIS. IEEE Transactions on Geoscience and Remote Sensing 30, 261–270. https://doi.org/10.1109/36.134076

Kaufman, Y.J., Tanre, D., 1992b. Atmospherically resistant vegetation index (ARVI) for EOS-MODIS. IEEE Transactions on Geoscience and Remote Sensing 30, 261–270. https://doi.org/10.1109/36.134076

Korhonen, L., Korpela, I., Heiskanen, J., Maltamo, M., 2011. Airborne discrete-return LIDAR data in the estimation of vertical canopy cover, angular canopy closure and leaf area index. Remote Sensing of Environment 115, 1065–1080. https://doi.org/10.1016/j.rse.2010.12.011

Lange, M., Dechant, B., Rebmann, C., Vohland, M., Cuntz, M., Doktor, D., 2017. Validating MODIS and Sentinel-2 NDVI Products at a Temperate Deciduous Forest Site Using Two Independent Ground-Based Sensors, in: Sensors.

Luvisi, A., Aprile, A., Sabella, E., Vergine, M., Nicolì, F., Nutricati, E., Miceli, A., Negro, C., Bellis, L.D., 2017. Xylella fastidiosa subsp. pauca (CoDiRO strain) infection in four olive (Olea europaea L.) cultivars: profile of phenolic compounds in leaves and progression of leaf scorch symptoms. Phytopathologia Mediterranea 56, 259-273–273. https://doi.org/10.14601/Phytopathol_Mediterr-20578

Martín, A., Zarco-Tejada, P.J., González, M.R., Berjón, A., 2007. Using Hyperspectral Remote Sensing to map grape quality in “Tempranillo” Vineyards affected by Iron deficiency Chlorosis.

Meggio, F., Zarco-Tejada, P.J., Miller, J.R., Martín, A., González, M.R., Berjón, A., 2008. Row Orientation and Viewing Geometry Effects on Row-structured Crops for Chlorophyll Content Estimation.

Montandon, L.M., 2009. The impact of soil properties on soil NDVI and the quantification of the green vegetation fraction (Ph.D.). University of Colorado at Boulder, United States -- Colorado.

Mura, M., Bottalico, F., Giannetti, F., Bertani, R., Giannini, R., Mancini, M., Orlandini, S., Travaglini, D., Chirici, G., 2018. Exploiting the capabilities of the Sentinel-2 multi spectral instrument for predicting growing stock volume in forest ecosystems. International Journal of Applied Earth Observation and Geoinformation 66, 126–134. https://doi.org/10.1016/j.jag.2017.11.013

Myneni, R.B., Marshak, A., Knyazikhin, Y., Asrar, G., 1991. Discrete Ordinates Method for Photon Transport in Leaf Canopies, in: Photon-Vegetation Interactions. Springer, Berlin, Heidelberg, pp. 45–109. https://doi.org/10.1007/978-3-642-75389-3_3

Niblack, W., 1986. An Introduction to Digital Image Processing, First English Edition edition. ed. Prentice Hall, Englewood Cliffs, N.J.

Noori, O., Panda, S.S., 2016. Site-specific management of common olive: Remote sensing, geospatial, and advanced image processing applications. Computers and Electronics in Agriculture 127, 680–689. https://doi.org/10.1016/j.compag.2016.07.031

North, P.R.J., 1996. Three-dimensional forest light interaction model using a Monte Carlo method. IEEE Transactions on Geoscience and Remote Sensing 34, 946–956. https://doi.org/10.1109/36.508411

Nutter, F.W., Esker, P.D., Netto, R.A.C., 2006. Disease Assessment Concepts and the Advancements Made in Improving the Accuracy and Precision of Plant Disease Data. Eur J Plant Pathol 115, 95–103. https://doi.org/10.1007/s10658-005-1230-z

Pearson, R.L., Miller, L.D., 1972. Remote Mapping of Standing Crop Biomass for Estimation of the Productivity of the Shortgrass Prairie. Presented at the Remote Sensing of Environment, VIII, p. 1355.

Peltzer, D.A., Köchy, M., 2001. Competitive Effects of Grasses and Woody Plants in Mixed-Grass Prairie. Journal of Ecology 89, 519–527.

Pinty, B., Verstraete, M.M., 1992. GEMI: a non-linear index to monitor global vegetation from satellites. Vegetatio 101, 15–20. https://doi.org/10.1007/BF00031911

Rahimzadeh-Bajgiran, P., Weiskittel, A.R., Kneeshaw, D., MacLean, D.A., 2018. Detection of Annual Spruce Budworm Defoliation and Severity Classification Using Landsat Imagery. Forests 9, 357. https://doi.org/10.3390/f9060357

Richardson, A.J., Wiegand, C.L., 1977. Distinguishing vegetation from soil background information. [by gray mapping of Landsat MSS data]. Photogrammetric Engineering and Remote Sensing.

Richter, R., Wang, X., Bachmann, M., Schläpfer, D., 2011. Correction of cirrus effects in sentinel-2 type of imagery. International Journal of Remote Sensing 32, 2931–2941. https://doi.org/10.1080/01431161.2010.520346

Rivera, J.P., Verrelst, J., Gómez-Dans, J., Muñoz-Marí, J., Moreno, J., Camps-Valls, G., 2015. An Emulator Toolbox to Approximate Radiative Transfer Models with Statistical Learning. Remote Sensing 7, 9347–9370. https://doi.org/10.3390/rs70709347

Rondeaux, G., Steven, M., Baret, F., 1996. Optimization of soil-adjusted vegetation indices. Remote Sensing of Environment 55, 95–107. https://doi.org/10.1016/0034-4257(95)00186-7

Roujean, J.-L., Breon, F.-M., 1995. Estimating PAR absorbed by vegetation from bidirectional reflectance measurements. Remote Sensing of Environment 51, 375–384. https://doi.org/10.1016/0034-4257(94)00114-3

Rouse, J.W., Jr., Haas, R.H., Schell, J.A., Deering, D.W., 1974. Monitoring Vegetation Systems in the Great Plains with Erts. NASA Special Publication 351, 309.

Saponari, M., Boscia, D., Altamura, G., Loconsole, G., Zicca, S., D'Attoma, G., Morelli, M., Palmisano, F., Saponari, A., Tavano, D., Savino, V.N., Dongiovanni, C., Martelli, G.P., 2017. Isolation and pathogenicity of Xylella fastidiosa associated to the olive quick decline syndrome in southern Italy. Scientific Reports 7, 17723. https://doi.org/10.1038/s41598-017-17957-z

Sauvola, J., Pietikäinen, M., 2000. Pietikainen, M.: Adaptive Document Image Binarization. Pattern Recognition 33, 225-236. https://doi.org/10.1016/S0031-3203(99)00055-2

Seem, R.C., 1984. Disease Incidence and Severity Relationships. Annual Review of Phytopathology 22, 133–150. https://doi.org/10.1146/annurev.py.22.090184.001025

Sibbett, G.S., Ferguson, L., 2005. Olive Production Manual. UCANR Publications.

Sisterson, M.S., Thammiraju, S.R., Lynn-Patterson, K., Groves, R.L., Daane, K.M., 2010. Epidemiology of Diseases Caused by Xylella fastidiosa in California: Evaluation of Alfalfa as a Source of Vectors and Inocula. Plant Disease 94, 827–834. https://doi.org/10.1094/PDIS-94-7-0827

Strona, G., Carstens, C.J., Beck, P.S.A., 2017. Network analysis reveals why Xylella fastidiosa will persist in Europe. Scientific Reports 7, 71. https://doi.org/10.1038/s41598-017-00077-z

Verhoef, W., 1984. Light scattering by leaf layers with application to canopy reflectance modeling: The SAIL model. Remote Sensing of Environment 16, 125–141. https://doi.org/10.1016/0034-4257(84)90057-9

White, S.M., Bullock, J.M., Hooftman, D.A.P., Chapman, D.S., 2017. Modelling the spread and control of Xylella fastidiosa in the early stages of invasion in Apulia, Italy. Biol Invasions 19, 1825–1837. https://doi.org/10.1007/s10530-017-1393-5

Whyte, A., Ferentinos, K.P., Petropoulos, G.P., 2018. A new synergistic approach for monitoring wetlands using Sentinels -1 and 2 data with object-based machine learning algorithms. Environmental Modelling & Software 104, 40–54. https://doi.org/10.1016/j.envsoft.2018.01.023

Yáñez-Rausell, L., Malenovský, Z., Rautiainen, M., Clevers, J.G.P.W., Lukeš, P., Hanuš, J., Schaepman, M.E., 2015. Estimation of Spruce Needle-Leaf Chlorophyll Content Based on DART and PARAS Canopy Reflectance Models. IEEE Journal of Selected Topics in Applied Earth Observations and Remote Sensing 8, 1534–1544. https://doi.org/10.1109/JSTARS.2015.2400418

Yang, W., Kobayashi, H., Suzuki, R., Nasahara, K.N., 2014. A Simple Method for Retrieving Understory NDVI in Sparse Needleleaf Forests in Alaska Using MODIS BRDF Data. Remote Sensing 6, 11936–11955. https://doi.org/10.3390/rs61211936

Zarco-Tejada, P.J., Camino, C., Beck, P.S.A., Calderon, R., Hornero, A., Hernández-Clemente, R., Kattenborn, T., Montes-Borrego, M., Susca, L., Morelli, M., Gonzalez-Dugo, V., North, P.R.J., Landa, B.B., Boscia, D., Saponari, M., Navas-Cortes, J.A., 2018a. Previsual symptoms of Xylella fastidiosa infection revealed in spectral plant-trait alterations. Nature Plants. https://doi.org/10.1038/s41477-018-0189-7

Zarco-Tejada, P.J., González-Dugo, M.V., Fereres, E., 2016. Seasonal stability of chlorophyll fluorescence quantified from airborne hyperspectral imagery as an indicator of net photosynthesis in the context of precision agriculture. Remote Sensing of Environment 179, 89–103. https://doi.org/10.1016/j.rse.2016.03.024

Zarco-Tejada, P.J., Hornero, A., Beck, P.S.A., Kattenborn, T., Kempeneers, P., Hernández-Clemente, R., 2019. Chlorophyll content estimation in an open-canopy conifer forest with Sentinel-2A and hyperspectral imagery in the context of forest decline. Remote Sensing of Environment 223, 320–335. https://doi.org/10.1016/j.rse.2019.01.031

Zarco-Tejada, P.J., Hornero, A., Beck, P.S.A., Kattenborn, T., Kempeneers, P., Hernández-Clemente, R., submitted. Chlorophyll content estimation in an open-canopy conifer forest with Sentinel-2A and hyperspectral imagery in the context of forest decline. Remote Sensing of Environment.

Zarco-Tejada, P.J., Hornero, A., Hernández-Clemente, R., Beck, P.S.A., 2018b. Understanding the temporal dimension of the red-edge spectral region for forest decline detection using high-resolution hyperspectral and Sentinel-2a imagery. ISPRS Journal of Photogrammetry and Remote Sensing 137, 134–148. https://doi.org/10.1016/j.isprsjprs.2018.01.017

Zarco-Tejada, P.J., Miller, J.R., Mohammed, G.H., Noland, T.L., Sampson, P.H., 2001. Estimation of chlorophyll fluorescence under natural illumination from hyperspectral data. International Journal of Applied Earth Observation and Geoinformation 3, 321–327. https://doi.org/10.1016/S0303-2434(01)85039-X

Zarco-Tejada, P.J., Morales, A., Testi, L., Villalobos, F.J., 2013. Spatio-temporal patterns of chlorophyll fluorescence and physiological and structural indices acquired from hyperspectral imagery as compared with carbon fluxes measured with eddy covariance. Remote Sensing of Environment 133, 102–115. https://doi.org/10.1016/j.rse.2013.02.003

Zhang, Y., Chen, J.M., Miller, J.R., Noland, T.L., 2008. Leaf chlorophyll content retrieval from airborne hyperspectral remote sensing imagery. Remote Sensing of Environment 112, 3234–3247. https://doi.org/10.1016/j.rse.2008.04.005

Zurita-Milla, R., Laurent, V.C.E., van Gijsel, J.A.E., 2015. Visualizing the ill-posedness of the inversion of a canopy radiative transfer model: A case study for Sentinel-2. International Journal of Applied Earth Observation and Geoinformation, Special Issue on “Advances in remote sensing of vegetation function and traits” 43, 7–18. https://doi.org/10.1016/j.jag.2015.02.003